USANS investigation of 100Cr6 double row ball bearings for automotive power transmission

Neutron Physics Laboratory - Neutron diffraction

Massimo Rogante

Proposal ID

465

Report regarding proposal "USANS investigation of 100Cr6 double row ball bearings for automotive power transmission".

Massimo Rogante, Rogante Engineering Office

The two (new and old) double row ball bearings were preliminarily cut to obtain 3 mm samples suitable to carry out the experiment, see Figure 1.

Fig. 1.

The steel samples scatter excessively. In low Q region the strong multiple scattering appeared, which significantly distorted SANS curves. It caused by to high scattering contrast (mainly – magnetic difference of scattering length densities between large austenite/martensite and ferrite grains) and large thickness of the samples. This scattering forms intense scattering background for high Q part, and it makes not possible to detect signs of degradation in the material. The small difference in intensity is due to slightly different thickness (the old sample is a little thinner than the new one), see Figure 2.

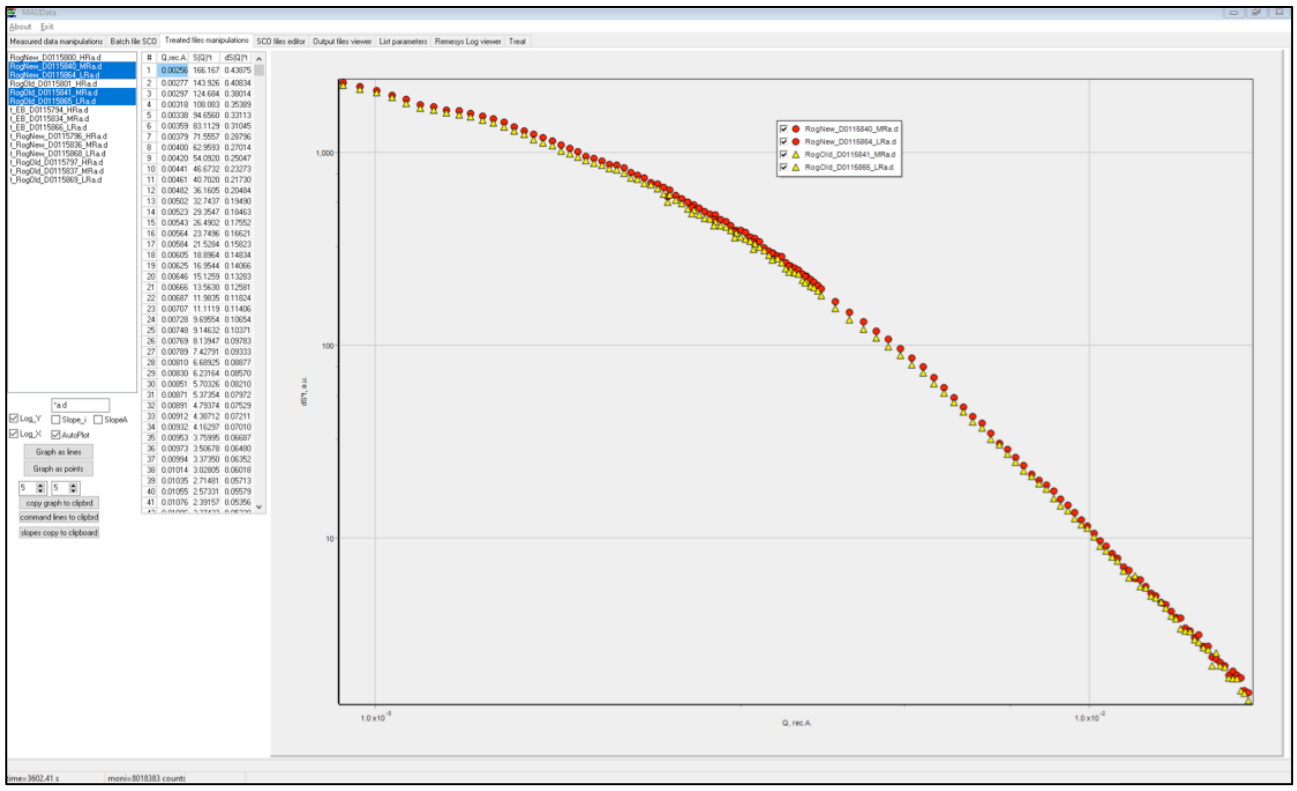

Fig. 2. (new sample – red, old sample – yellow).

Effects of radiation-induced damage on light ions diffusion in ISOL-related targets

Laboratory of Tandetron

Antonino Cannavó

Proposal ID

530

Report regarding proposal "Effects of radiation-induced damage on light ions diffusion in ISOL-related targets"

Antonino Cannavó, Vladimír Havránek and Jiří Vacík

Methods

In the experiment, molybdenum foils with a thickness of 50 μm were implanted at room temperature with $^6Li^+$ ions with energy 390 keV with a fluence of about 10^{16} cm^{-2}. The implantation was carried out at the Helmholtz-Zentrum Dresden-Rossendorf (HZDR) at the 3 MV Tandem accelerator. The $^6Li^+$ ion beam current density was about 10-25 nA/cm^2 corresponding to the thermal power density between 4 to 12 mW/cm^2. After implantation of $^6Li^+$ (in HZDR Dresden), a part of the Mo(^{6}Li) samples was irradiated by 12 MeV $^{12}C^{4+}$ ions with a fluence of 10^{14} cm^{-2} at the 3 MV Tandetron accelerator in the NPI Řež. The aim was to generate radiation defects in the Mo(^{6}Li) foils, which should lead (due to radiation-induced diffusion) to redistribution of the ^{6}Li dopants. However, because of the possible heating effect, caused by the $^{12}C^{4+}$ ion bombardment, it was necessary to prevent the sample temperature from rising, which would otherwise also induce unwanted Li diffusion. Therefore, the Mo(^{6}Li) foils were irradiated only with a low current of about 10 nA/cm^2, so the temperature on the sample (measured in situ by a K-type thermocouple, did not exceed 40 °C throughout the monitoring period.

Results

The ^{6}Li depth profiles in the Mo(^{6}Li) foils before (Pristine) and after $^{12}C^{4+}$ irradiation (Irradiated) were measured by the NDP method at the research reactor LVR-15 in Řež (operated by the Research Center Řež). When determining the residual energies of α-particles and tritons for thermal neutron-induced reaction, the depth position of their parent atoms (^{6}Li) in the Mo(^{6}Li) foils can be evaluated. For this purpose, the MC LIBOR code was developed, using the SRIM database, which allows reconstruction of the ^{6}Li depth profiles in solids.

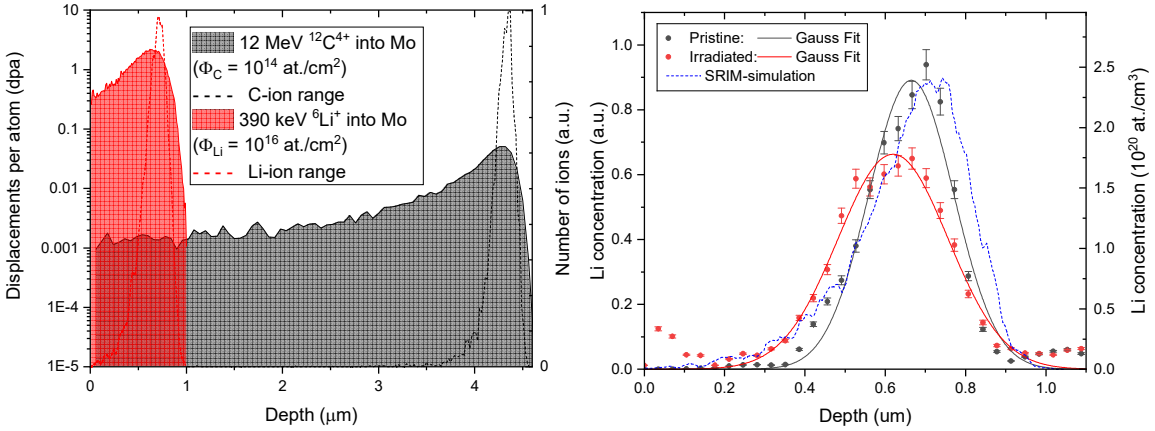

Figure 1: Left: SRIM simulations of ions range (dashed lines) and damage in dpa units (area under curves) for 390 keV $^6Li^+$ and 12 MeV $^{12}C^{4+}$ ions, in red and black colors, respectively. Right: SRIM simulation and Li-depth profiles for Pristine and Irradiated samples with the corresponding Gaussian fits.

Irradiation conditions in both 390 keV $^6Li^+$ ion implantation and 12 MeV $^{12}C^{4+}$ ion irradiation were first inspected by the SRIM code. Fig. 1 (left) shows the result of the SRIM simulation. The simulation shows that the range of $^6Li^+$ ions (660 nm) in Mo is significantly smaller than that of $^{12}C^{4+}$ ions (4280 nm), and that the radiation damage (expressed as the equivalent displacement dose, D), caused by the carbon ion bombardment, is approximately the same ($\sim 1.5 \times 10^{-3}$ dpa) throughout the entire passage of the $^6Li^+$ ions in Mo. On the other hand, the destructive effect of Li ions is concentrated on the narrow subsurface region of the Mo foil, and for a thickness T as less as 660 nm, the D is greater (~2.16 dpa) than for $^{12}C^{4+}$ ions. The deconvolution of the NDP spectra into Li-depth profiles is shown in Fig. 1 (right). The FWHM parameter, characterizing the Gaussian-like depth profile distributions, increased from the original value of 249 nm (for Pristine) to 320 nm (for Irradiated), which demonstrates the RID effect after bombardment (12 MeV $^{12}C^{+4}$, $\Phi_C = 10^{14}$ cm^{-2}). In addition, the centroid of the Gaussian curves has shifted from 665 nm to 619 nm.

Characterization of lithium mobility in glass-ceramic LICGC solid electrolyte

Neutron Physics Laboratory - Nuclear analytical methods with neutrons

Antonino Cannavó

Proposal ID

531

Report on the experiment:

Characterization of lithium mobility in glass-ceramic LICGC solid electrolyte

Antonino Cannavó, Ivo Tomandl, Giovanni Ceccio, Jiří Vacík.

The NDP method proved to be a unique tool for the study of lithium transportation (migration and diffusion) in the Solid Electrolyte (SE). The experiment has pointed out the formation of a lithium depleted region in the interface between the LICGC SE and Au/Cu current collector. In particular, it was observed how the phenomenon occurs in relation to the applied voltage and time.

The formation of the Li -depleted region at the SE/Cu interface results in a variation of the NDP spectra in the channel range between 850 and 1000. This region of the spectrum corresponds to the most energetic tritons, generated close by the sample surface: Fig. 1a shows that the longer the applied voltage the smaller the area subtended by the spectrum, clearly pointing at the depletion of lithium atoms.

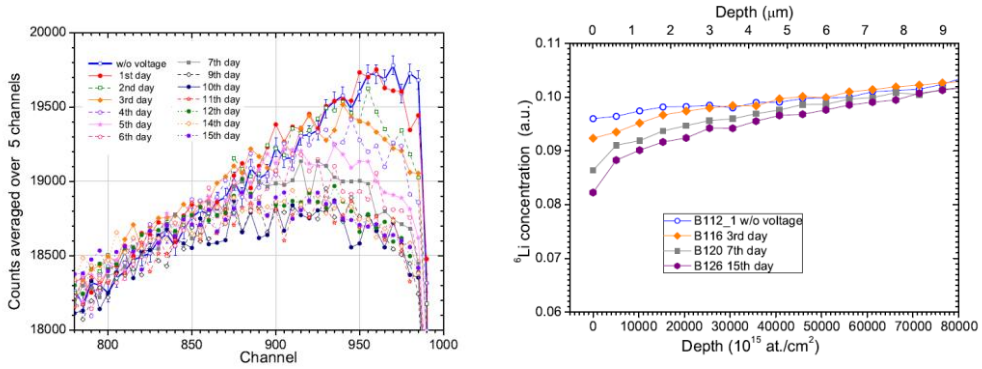

Fig.1: a) detail of the NDP spectra in the channel range between 800 and 1000; all the spectra are normalized to the same neutron fluence. b) corresponding Li-depth profile evaluated by LIBOR simulation code.

Data analysis was performed by using the LIBOR simulation code [1]. Fig. 1b shows that a consistent trend is being observed in the Li-depth profile estimated in the selected area as well.

The collected data have been used in the preparation of a paper, that now is under consideration for publication in an impacted journal.

This is the first experiment to describe the actual distribution of Li atoms in the process of forming the space charge layer. Further steps to better understand the mechanism of lithium migration and diffusion in LICGC will involve new voltage cycling strategies (negative biasing), as well as, the combination of NDP data with complementary methodologies, e.g. Rutherford Backscattering Spectroscopy or gamma-rays Spectroscopy, for a comprehensive understanding of the Li-depleted region formation at the SE interface.

References

[1] Hnatowicz, V., J. Vacik, and D. Fink. "Deconvolution of charged particle spectra from neutron depth profiling using Simplex method." Review of Scientific Instruments 81.7 (2010): 073906.

Crystal and magnetic structure of La18M3Co28 (M=Mg,In,Cd)

Neutron Physics Laboratory - Neutron diffraction

Vitalii Shtender

Proposal ID

467

Report regarding proposal “Crystal and magnetic structure of $La_{18}M_3Co_{28}$ (M=Mg,In,Cd)”

V. Shtender, M. Sahlberg, Uppsala University, Sweden

Instrument responsible: C. Hervoches P. Beran, Nucl. Physics Inst., Rez, Czech Republic

The aim was to investigate crystal as well as magnetic structures of the $La_{18}M_3Co_{28}$ (M = Mg, Cd and In) compounds. There was need to confirm the XRD first results on incommensaturate crystal structures and resolve their different magnetic properties.

Neutron powder diffraction experiments were performed on different samples of general $La_{18}Mg_3Co_{28}$ composition at 298 K using the MEREDIT instrument. The motivation for the experiments was to investigate the possible large displacement of Mg.

The extracted data is still under evaluation but preliminary results propose modulated structure of the $La_{18}Mg_3Co_{28}$. Observed and calculated neutron powder diffraction profiles are shown in fig. 1. The preliminary proposed incomensurated structure which is along the c-axis with a Mg atom inside the tunnel. The maximum entropy method (MEM) was applied to calculate nuclear density of the unit cell. The output of the calculation is shown in Fig 1. The cut-off intensity was set to 0.5 fm. The area of disordered space where Mg atoms could be located is clearly visible. Other atoms don’t show anisotropy behavior.

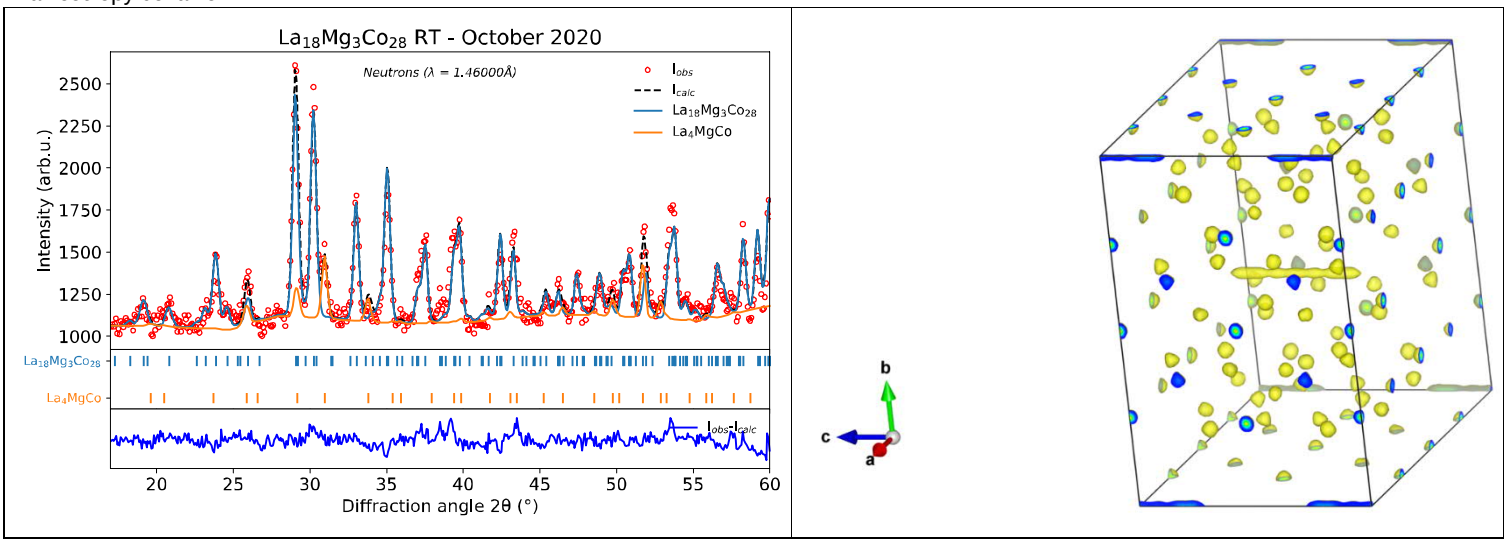

Fig 1. Refinement of the NPD for $La_{18}Mg_3Co_{28}$ at 298K and proposed structure with the nuclear density.

Neutron depth profiling and PIXE/PIGE comparative study on Li distribution in mixed cathodes of oxid

Neutron Physics Laboratory - Nuclear analytical methods with neutrons

Stefan Seidlmayer

Proposal ID

532

Report regarding proposal “Neutron depth profiling and PIXE/PIGE comparative study on Li distribution in mixed cathodes of oxide (LLZO-LCO) based all-solid-state batteries”

Stefan Seidlmayer, Thien-An Pham, Ivana Pivarnikova, Lukas Grossmann, MLZ (Heinz Maier-Leibnitz Zentrum, Technical University Munich, Germany)
Martin Finsterbusch, Forschungszentrum Jülich GmbH, Institut für Energie- und Klimaforschung (IEK), Jülich, Germany
Antonino Cannavo, Giovannia Ceccio, Jiri Vacik, Nucl. Physics Inst. CAS, Rez, Czech Republic

Here we investigated samples of all-solid state battery cells brought to different states of charge and a reference sample being a pure LLZO pellet of solid electrolyte material. The conducted measurements used the NDP spectrometer in the Center of Accelerators and Nuclear Analytical Methods (CANAM) infrastructure of the Nuclear Physics Institute (NPI) CAS in Rez, Czech Republic. Due to the Covid-19 pandemic, NPI instrument responsible scientists carried out the experiments remotely. The measurements used two setups: the A-Line with an inserted 2.8 µm Macrofol filter and B-Line without any filter. Calibration to energy and Li-concentration was performed with a ^{6}LiF standard (see fig. 1) measured in both Line setups. Data analysis for the complex full cell samples is ongoing. The expected nuclear reaction of interest for the lithium depth profiles is ^{6}Li(n, ^{3}H)^{4}He, which generates two particles of interest, namely Triton ($^{3}H^{+}$) and alpha ($^{4}He^{2+}$) particles with different recoil energies of 2727 keV (^{3}H) and 2055 keV (^{4}He), respectively. The lithium depth profiles are calculated with the N4DP software package [1, 2], which applies the stopping power of the atomic composition of the sample simulated by the SRIM software [3] on the energy calibrated data set. The evaluation assumes a constant average density across the layers of interest. The abundance of ^{6}Li was set to the natural value of 7.59% according to IUPAC [4]. Figure 2 shows the obtained Li depth-profiles obtained by using the N4DP software package implementing SRIM-data for the data treatment. For B-Line, the data treatment assumed an 80 nm thick Si dead layer of the detector and for A-Line an additional 2.8 µm thick Macrofol passive layer. Finally, we applied a sample specific calculation for the active layer SRIM-profile. For sample #5, a pellet of pure LLZO material we assumed a homogenous average composition $Li_{6.6}Al_{0.15}La_3Zr_{1.58}Hf_{0.02}Ta_{0.4}O_{12}$ with an average density of 4.924 g/cm^3. Preliminary inspection of the data suggests a very homogenous Li distribution. The accessible depth of the LLZO pellet is approximately 20 µm. Interestingly, there is an unexpected surface peak in both signals, i.e. Triton and Alpha particles, indicating a possible Li-gradient up to a depth of 300 – 400 nm, which could point towards a concentration gradient in the LLZO-particles, decreasing from shell to core.

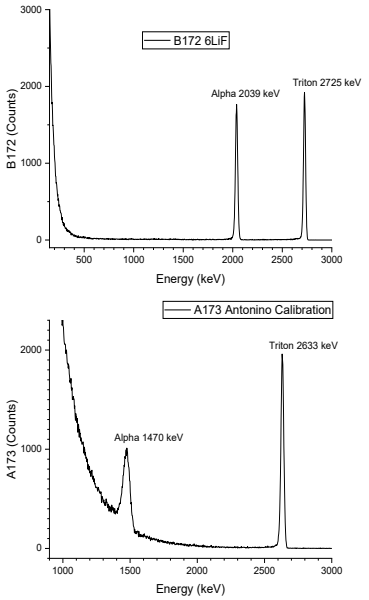

Fig. 2: NDP spectra of the ^{6}LiF standard measured on the A- and B-Lines.

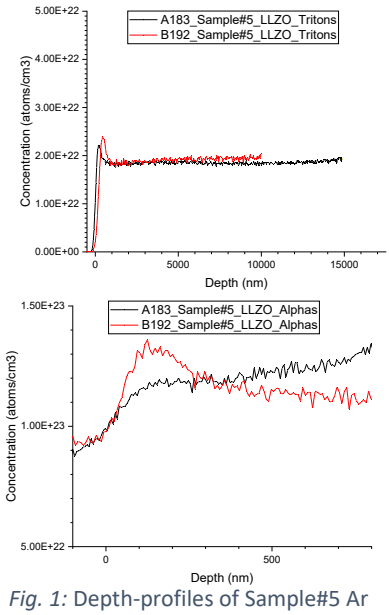

Fig. 1: Depth-profiles of Sample#5 Ar annealed LLZO-Pellet. Top: Triton particles; Bottom: Alpha particles;

References

1. Werner, L., Trunk, M., Gernhäuser, R., Gilles, R., Märkisch, B. and Révay, Z., 2018, Nuclear Instruments and Methods in Physics Research Section A: Accelerators, Spectrometers, Detectors and Associated Equipment, 911, 30-36.
2. Trunk, M., Wetjen, M., Werner, L., Gernhäuser, R., Märkisch, B., Révay, Z., Gasteiger, H. A. and Gilles, R., 2018, Materials Characterization, 146, 127-134.
3. Ziegler, J. F., Ziegler, M. D. and Biersack, J. P., 2010, Nuclear Instruments & Methods in Physics Research Section B-Beam Interactions with Materials and Atoms, 268(11-12), 1818-1823.
4. Meija, J., Coplen, T. B., Berglund, M., Brand, W. A., Bièvre, P. D., Gröning, M., Holden, N. E., Irrgeher, J., Loss, R. D., Walczyk, T. and Prohaska, T., 2016, Pure and Applied Chemistry, 88(3), 293-306.

Investigate the structures of Na-ion cathode materials

Neutron Physics Laboratory - Neutron diffraction

Neelima Paul

Proposal ID

534

Research question: In our work, we want to elucidate the influence of the charge ordering in the transition metal slab on the sodium/vacancy ordering within the sodium slab of the material. We have synthesised both phase-pure materials, P2-$Na_xNi_{1/3}Mn_{2/3}O_2$ and P2-$Na_{2/3}Ni_{1/4}Mn_{3/4}O_2$, and used electrochemical methods as well as X-ray diffraction to investigate sodium/vacancy orderings in these materials. Both materials exhibit sodium/vacancy orderings at the reported compositions. To characterise the ordering of manganese and nickel within the transition metal slab, neutron powder diffraction measurements have been performed at Meredit.

Obtained data and analysis: The obtained neutron powder diffraction patterns of the three samples measured at Meredit, $Na_{2/3}Ni_{1/3}Mn_{2/3}O_2$, $Na_{2/3}Ni_{1/4}Mn_{3/4}O_2$ and $Na_{0.59}Ni_{1/4}Mn_{3/4}O_2$, are represented in Figure 1.

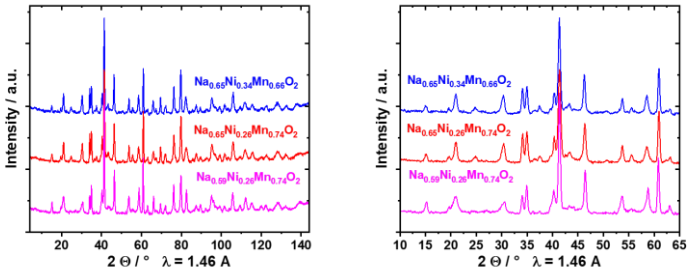

Figure 1: NPD patterns measured at Meredit. (left) complete data set, (right) zoom-in for identification of superstructure.

The diffraction patterns of all three samples exhibit additional reflections (between 18°–28° 2Θ) compared to X-ray patterns that can be indexed using the superstructure with propagation vector ***k***=(1/3 1/3 0). This superstructure is created by ordering the nickel-manganese in the honeycomb sub-lattice. The order is revealed in diffraction data thanks to the different neutron scattering lengths of Ni and Mn.
Three different stacking sequences of the identified nickel-manganese orderings are reported in literature[8,9]: (i) A-A stacking, (ii) A-B stacking or (iii) a mixture of both (stacking faults). All three options were examined, and the analysis suggests that the A-B stacking dominates.

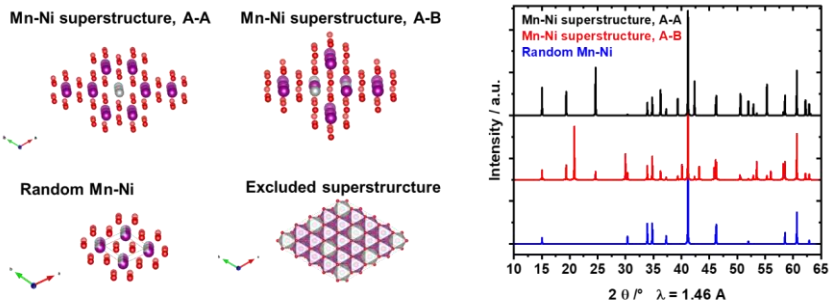

Figure 2: (left) Possible transition metal superstructures and stacking sequences. (right) Simulated NPD data using PowderCell. Refinement of the NPD data suggests that the honeycomb Mn-Ni ordering with A-B stacking sequence is dominant in all three samples.

Additional broadening of (10*l*) reflections is identified in NPD and XRD data. This anisotropic broadening most likely results from two-dimensional stacking faults within the layered structure. We are currently evaluating possible two-dimensional stacking faults and implementing these in the software Faults[10] (part of FullProf). The simultaneous analysis of NPD and XRD data with these models is ongoing.
So far, the best results are obtained by incorporating (2/3 1/3 1/2 translations, leading to a different prismatic sodium environment and different stacking of the transition metals.

Investigation of Li distribution in Si/C composite anodes from Li-ion batteries at selected SOHs

Neutron Physics Laboratory - Nuclear analytical methods with neutrons

Ivana Pivarníková

Proposal ID

536

Experimental report for the Proposal ID 536:

Investigation of Li distribution in Si/C composite anodes from Li-ion batteries at selected SOHs

Ivana Pivarníková, Neelima Paul, Ralph Gilles (Heinz Maier-Leibnitz Zentrum (MLZ), Technical University Munich, Germany)
Marius Flügel, Christin Hogrefe, Thomas Waldmann (Zentrum für Sonnenenergie- und Wasserstoff- Forschung Baden-Württemberg (ZSW), Ulm, Germany)
Jiří Vacík (Nuclear Physics Institute, Rez, Czech Republic)

Neutron depth profiling measurements of Si/Graphite (Si 3.53 wt.%, C 96.47 wt.%, 1.58 g/cm^3) electrodes extracted from Li-ion batteries were performed at the T-NDP instrument. The electrodes were at different states of health (SOH) and previously aged under various conditions in order to investigate the influence of these parameters on the lithium depth profiles. The following 4 samples were measured: B146 (fresh electrode, SOH 100%), B147 (SOH 90%, aging at 45°C, with SEI formation), B148 (SOH 76%, aging at 45°C, with SEI formation), and B149 (SOH 60%, aging at 0 °C, with induced Li plating). Additionally, 3 different reference samples were measured: B150 (^{6}LiF), which was used for energy calibration, B152 (NIST standard RR4N16, 1.094E16 atom/cm^2 of ^{10}B atoms), which was used for quantity calibration, and B151 ($LiNbO_3$, 417 nm), which was used as an additional reference for crosschecking the analysis. The nuclear reaction of interest for the neutron depth profile is ^{6}Li(n,^{4}He)^{3}H, which creates two particles of interest: triton (^{3}H) and alpha (^{4}He) with their respective recoil energies of 2727 keV (^{3}H) and 2055 keV (^{4}He). For the thin reference sample ^{6}LiF, the signal is well defined and therefore can be used for energy calibration, as we can observe on the energy spectrum in Fig. 1a. In Fig. 1b, we can observe the energy spectra of $LiNbO_3$. For the NIST standard sample, the reaction of interest is ^{10}B(n,^{4}He)^{7}Li and we can observe the energy spectra in Fig. 1c. The peak positions are shifted in comparison to the theoretical values of the reactions due to implantation of ^{10}B into the Si substrate. However, this does not affect the suitability of the sample for quantity calibration of the Li content.

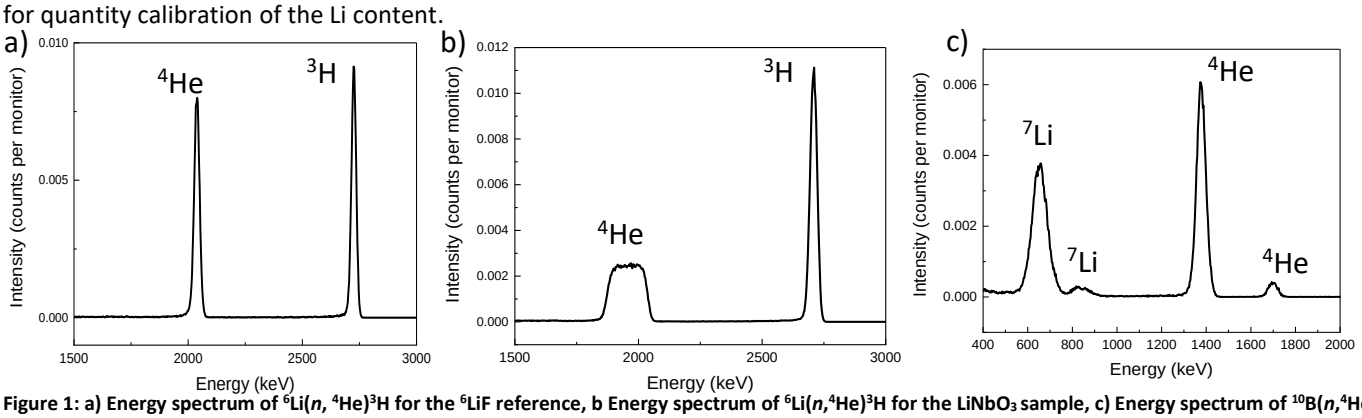

Figure 1: a) Energy spectrum of ^{6}Li(n, ^{4}He)^{3}H for the ^{6}LiF reference, b Energy spectrum of ^{6}Li(n,^{4}He)^{3}H for the $LiNbO_3$ sample, c) Energy spectrum of ^{10}B(n,^{4}He)^{7}Li for the NIST boron standard.

The depth profile analysis is done by N4DP software [1], which uses the energy loss of ions in matter calculated by the SRIM software [2] on the energy-calibrated data. A constant average density across the various layers is assumed for each sample. A natural isotopic abundance of 7.59% for ^{6}Li is assumed to calculate the total lithium concentration [3]. We can observe the energy spectra of our 4 measured samples in Fig. 2a. There is a clear overlap of alpha and triton signal, because of the higher thickness of electrodes (≈80 µm). Therefore, the available depth for our measurements is limited to approximately 16 µm (corresponding to a triton spectrum between 2075 and 2055 keV), as seen in Figure 2b, which also shows the final depth profiles of the Li distribution in the electrodes. We can observe increasing Li concentration with a decreasing SOH of the electrodes. Moreover, the highest peak (B149) corresponds to the electrode with charging conditions inducing Li-plating on the electrode surface, as was expected. As planned, these results were compared with the results from GD-OES (glow discharge optical emission spectroscopy) depth profiling method. It turns out that the Li depth profiles from both methods are in good agreement. The publication of these results is currently in preparation.

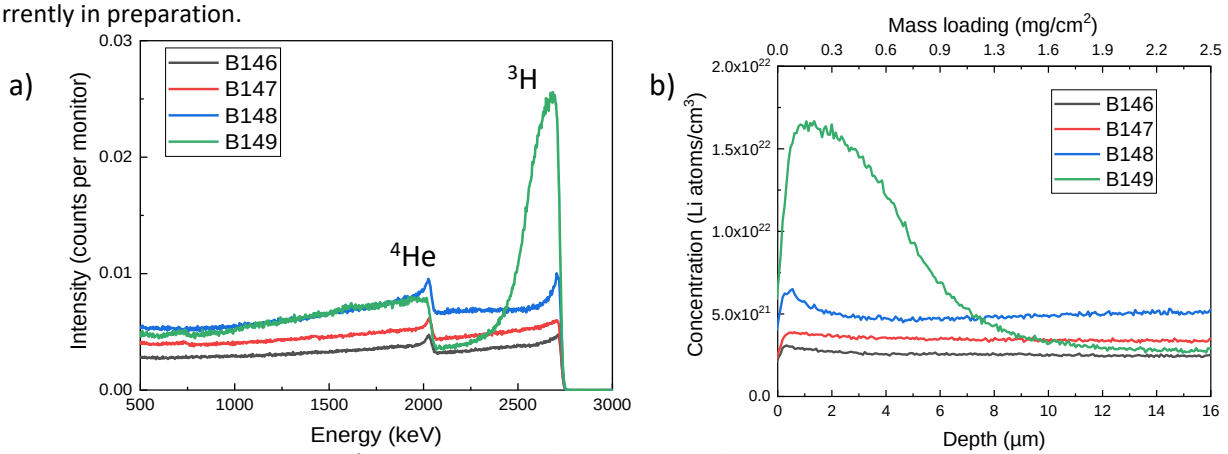

Figure 2: Results for four different types of Si/Graphite electrodes: a) Energy spectra, b) Lithium concentration profiles as a function of electrode depth.

[1] Trunk, M., Wetjen, M., Werner, L., Gernhäuser, R., Märkisch, B., Révay, Z., Gasteiger, H. A. and Gilles, R., 2018, Materials Characterization, 146, 127-134.
[2] Ziegler, J. F., Ziegler, M. D. and Biersack, J. P., 2010, Nuclear Instruments & Methods in Physics Research Section B-Beam Interactions with Materials and Atoms, 268(11-12), 1818-1823
[3] Meija, J., Coplen, T. B., Berglund, M., Brand, W. A., Bièvre, P. D., Gröning, M., Holden, N. E., Irrgeher, J., Loss, R. D., Walczyk, T. and Prohaska, T., 2016, Pure and Applied Chemistry, 88(3), 293-306.

Macroporous PDMS decorated with organic and inorganic materials for application in microelectronics

Laboratory of Tandetron

Mariapompea Cutroneo

Proposal ID

473

Report

A hybrid material incorporating gold nanoparticles (Au-NPs) in polydimethylsiloxane (PDMS) has been synthesized. Gold nanoparticles gained wide interest for their optical, chemical and physical properties, such as surface plasmon oscillations resonant absorption, chemical structure, imaging and sensing. Au-NPs can be conjugated with several functionalizing agents, such as polymeric chains, improving their properties and performances. PDMS composites with weight percentages ranging between 0.1 and 0.2% of spherical Au-NPs (10 nm diameter), were produced. The surface morphology was investigated by atomic force microscopy (AFM) and wetting ability analyses see **Figure 2**.

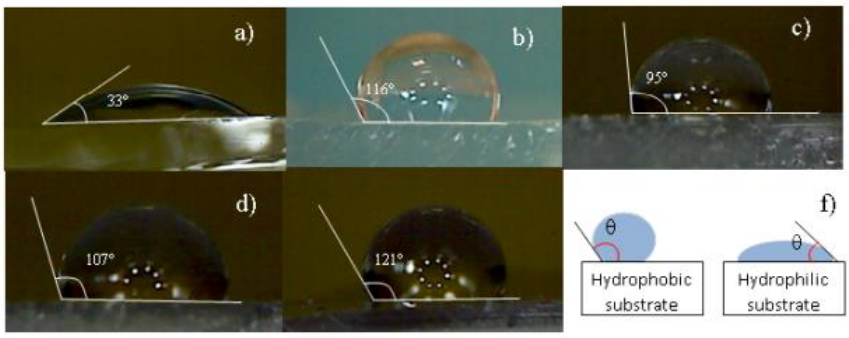

Figure 2. *Optical images for wettability measurements of virgin Glass (a), virgin PDMS (b), PDMS containing 0.1% wt NPs (c) PDMS containing 0.2% wt wet Au-NPs (d) PDMS containing 0.2% wt dried Au-NPs (e) and schematic representation of water molecules on different substrates (d).*

The presence of structures inside both virgin and hybrid PDMS containing Au-NPs was preliminary investigated by Small Angle X-ray Scattering (SAXS). The optical performance of such hybrid material was studied by UV-VIS spectroscopy, in transmission mode.

Polymers containing metal nanoparticles have gained high interest in the optical field, due to their special optical properties, such as dichroism, switching and controlled absorption coefficient. The optical responses of Au-NPs embedded in PDMS films are connected to the Au-NPs features, which result from the adopted method. The PDMS network, does not protect the gold nanoparticles from aggregation as observed in the present study. The changes in the morphological and optical properties of the matrix are related to the presence of the Au-NPs dopants in PDMS working as links uniformly distributed in the polymer. The appearance of pink and violet PDMS-AuNPs composites suggests the presence of Au-NPs aggregates with different size, as confirmed by SAXS and AFM analyses and optical microscopy.

The UV-Vis measurement shows the maximum peak absorption at around 517 nm–528 nm indicating Au-NPs with size ranging between 10 nm and 60 nm in the investigated samples.

The sample exhibiting higher absorption is the PDMS containing 0.2 wt% of Au-NPs due to less aggregation of the fillers and consequent higher number of NPs per volume of matrix. The presence of Au NPs in PDMS improves the absorbance of the matrix as observed also during the laser irradiation of the sample leading to the enhancement of the emitted ion energy, electron density and plasma temperature. It is established that the higher the size of Au NPs is the higher the temperature in the surrounding area and the longer the time to reach the thermal equilibrium. Work is in progress to investigate the thermal behaviour of the PDMS containing Au-NPs, which is crucial for the control of the temperature distribution for applications in metallic micro- and nano-fabrication process by direct laser writing and ion beam writing but also for material growth, material absorption control, cancer treatment and controlled drug release.

Publications:

[1] Cutroneo M.; Havranek V.; Mackova A.; Malinsky P.; Silipigni L.; Slepicka P.; Fajstavr D.; Torrisi L., Synthesis of porous polydimethylsiloxane gold nanoparticles composites by a single step laser ablation process, International Journal of Molecular Sciences 2021

[2] Cutroneo, M.; Havránek, V.; Semián, V.; Torrisi, A.; Macková, A.; Malinský, P.; Silipigni, L.; Slepička, P.; Fajstavr, D.; Torrisi, L. (2021) Porous polydimethylsiloxane filled with graphene-based material for biomedicine. Journal of Porous Materials. 28, 1481-1491.

[3] Cutroneo, M.; Havránek, V.; Macková, A.; Malinský, P.; Torrisi, A.; Silipigni, L.; Slepička, P.; Fajstavr, D.; Torrisi, L. (2021) The characterisation of polydimethylsiloxane containing gold nanoparticles as a function of curing time. Surface and Interface Analysis. 53(7), 618-626. doi: 10.1002/sia.6948

[4] Cutroneo, M.; Havránek, V.; Torrisi, A.; Macková, A.; Malinský, P.; Slepička, P.; Sofer, Z.; Torrisi, L. (2020) Polydimethylsiloxane-graphene oxide composite improving performance by ion beam irradiation. *Surface and Interface Analysis. 52*(12), 1156-1162. doi: 10.1002/sia.6882

Unveiling the Lithium Depth Profile Upon Lithiation of Silicon-Based Anodes

Neutron Physics Laboratory - Nuclear analytical methods with neutrons

Lukas Grossmann

Proposal ID

538

Report regarding proposal ID 538: “Unveiling the Lithium Depth Profile Upon Lithiation of Silicon-Based Anodes”

Lukas Grossmann, Thien-An Pham, Stefan Seidlmayer, Phillip Rapp, and Ralph Gilles, Technical University of Munich (TUM), Germany
Antonino Cannavo, Giovanni Ceccio, and Jiri Vacik, Nuclear Physics Institute in Rez, Czech Republic

The usage of silicon as anode material in Lithium Ion Batteries (LIB) would lead to higher capacities as compared to common graphite anodes. However, the high volume increase of Si during lithiation leads to a low cycling stability.[1] One strategy to overcome this problem is the partial lithiation to ~30%, which results in a significant gain in cycling stability while maintaining a high capacity.[2] Homogeneous lithiation across the electrode is believed to be beneficial for the cycling stability since the stress caused by the increase in volume is evenly distributed.

We use thermal Neutron Depth Profiling (NDP) on extracted anodes to investigate the Li depth distribution after their formation and lithiation. The NDP method utilizes an intense 6Li(n, α)t reaction with a high cross section of 940 barns to measure the Li concentration vs. depth. Thereby, we use an electrode coating chemistry based on 70 wt.% of micrometer-sized Si particles. Additionally, we study the formation with and without $LiNO_3$ as electrolyte additive as it can significantly increase the cycling stability of these anodes.[3] Electrodes (Si-rich coating on Cu-collector) were packed in pouch bags with 7.6 µm thick Kapton windows to prevent contact with air and to filter out $^4He^{2+}$-particles during NDP, resulting in pure $^3H^+$-spectra. The samples were remeasured without the pouch bag after a short (few minutes) exposure to air to attain also the $^4He^{2+}$-signal.

The experiments were carried out using the NDP spectrometer in the Center of Accelerators and Nuclear Analytical Methods (CANAM) infrastructure of the Nuclear Physics Institute (NPI) in Rez, Czech Republic. The experiments had to be performed remotely due to the Covid-19 pandemic and were operated by the instrument responsible scientists.

Fig. 1 summarizes the preliminary results. The Li depth profiles are calculated based on the stopping power of the atomic composition of the electrode coating using the SRIM software.[4] In the evaluation, a constant (experimentally determined) density across the coating was assumed. The abundance of ^6Li was set to be 7.56% according to IUPAC.[5] All depth profiles measured with the Kapton filter show a homogeneous Li concentration (Fig. 1a). The low Li concentration from the pristine sample (i.e. with no electrochemical treatment) originates from the LiPAA binder used in the electrode coating. After formation, the Li concentration becomes five times higher resulting from Li irreversibly bound in the solid-electrolyte interface (SEI), which formed during the formation of the cell. With increasing lithiation state the Li concentration consistently increases. The drop in Li concentration at greater depths indicates the end of the coating. The inflection points are assumed to be the interface between the Li-containing Si-rich coating and the Cu collector. The coating was prepared homogeneously with a thickness of ~25 µm. However, the lithiation process caused a significant swelling of the coating layer, as evident from the broadening of the NDP depth profiles (see red lines and arrows in Fig. 1a). After unpacking and measuring the electrodes without the filter, the depth profiles slightly changed (Fig. 1b). It should be noted, that these profiles only make sense until the onset of the $^4He^{2+}$-signal between 30 and 40 µm. Interestingly, a dominant surface peak occurs which is an effect that has to be further evaluated. However, it indicates an enrichment of Li on the electrode surface. Furthermore, the surface peak is followed by a lowered Li concentration up to around 10 µm. Our first interpretation is that this dip is due to oxidation of the lithiated silicon. Fig. 1c compares the depth profiles of the electrodes after formation, whereby in one of the samples $LiNO_3$ was dissolved in the electrolyte as an additive. The depth profiles show a higher Li concentration in the SEI of the sample where the formation was conducted with the additive. Moreover, the intensity of the surface peaks differs. Appropriate complementary techniques as well as electrochemical measurements will be necessary to further interpret these results.

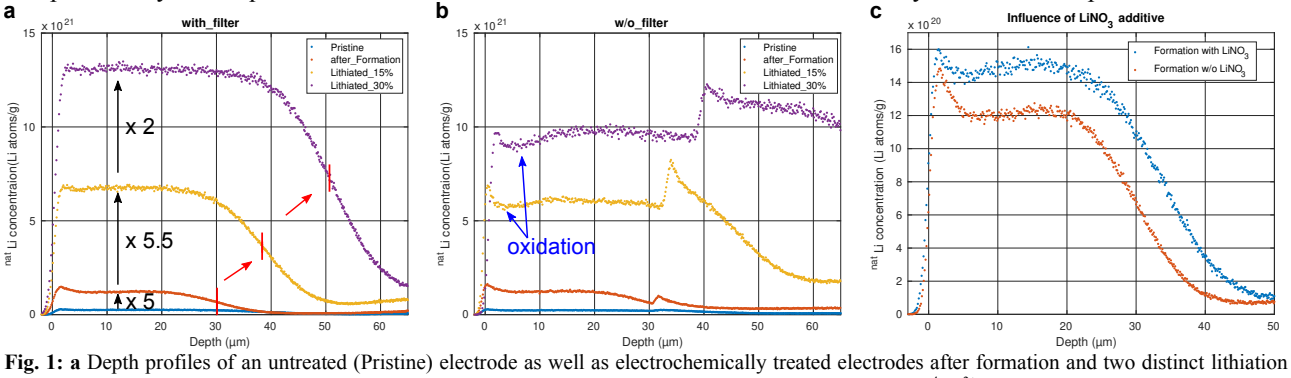

Fig. 1: a Depth profiles of an untreated (Pristine) electrode as well as electrochemically treated electrodes after formation and two distinct lithiation steps. These samples were measured through a 7.6 µm thick Kapton foil which acted as a stop-filter for the $^4He^{2+}$-particles and additionally prevented air contact of the sample prior to measurement. The swelling of the electrodes is indicated by the red lines and arrows. **b** Same samples as in a, but this time without a filter and a short air contact of the electrodes for a few minutes. The dips in the profiles ranging from appr. 2 to 10 µm as indicated by the blue arrows are interpreted as oxidation effects. **c** Comparison of two electrodes after the electrochemical formation step, once with $LiNO_3$-additive dissolved in the electrolyte and once without. These measurements were performed with a Kapton foil filter.

References

[1] Gonzalez, Joseph, et al. Journal of Power Sources 269 (2014): 334-343.
[2] Jantke, Dominik, et al. Journal of The Electrochemical Society 166.16 (2019): A3881.
[3] Haufe, Stefan, Rebecca Bernhard, and Jürgen Pfeiffer. Journal of The Electrochemical Society 168.8 (2021): 080531.
[4] Ziegler, James F., et al. Nuclear Instruments and Methods in Physics Research Section B 268.11-12 (2010): 1818-1823.
[5] De Laeter, John R., et al. Review 2000 (IUPAC Technical Report)." Pure and applied chemistry 75.6 (2003): 683-800.

Investigating pore evolution in Li & Li-CNT composite anodes

Neutron Physics Laboratory - Neutron diffraction

Neelima Paul

Proposal ID

539

Proposal # 539: Investigating pore evolution in Li & Li-CNT composite anodes

Sample description: Sample FGA, FGB, FGC and FGD are pouch bags containing Li pristine, Li cycled, Li-CNT pristine and Li-CNT cycled thin films, respectively. CNT is a short form for carbon nanotubes. We have an empty pouch bag (sample FG0) for background subtraction and a bag with pure CNTs (Sample FG1)

Instrument set-up: USANS measurements were conducted at MAUD facility – double bent crystals SANS installed at LVR-15 reactor in Rez near Prague. The samples were installed perpendicular to the incident neutron beam as shown in Fig. 1 and measured at three instrumental resolutions (high, medium and low) to cover a Q range from 0.01 to 0.0001 $Å^{-1}$. This should ideally allow investigations of lateral structures in the size range 20 nm - 2 µm. The neutron beam was focused on the sample center and the beam footprint on the sample was 15x4 mm^2. As the scattering was quite weak, each sample was measured about 24 hours in Dec 2021.

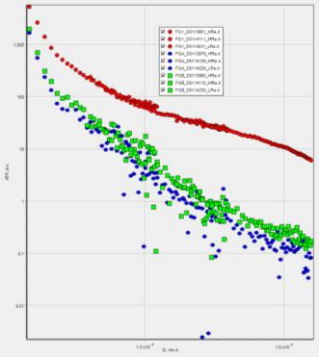

Fig. 1. USANS data of samples FG1, FGA, FGB (background subtracted using FG0)

Results: We wanted to gain information on pore evolution within these Li containing thin films upon cycling over the entire sample volume on the nano- and microscale with VSANS at MAUD. The USANS data shows that porous CNT powder sample (FG1) scatters the most due to higher contrast between CNT and air. The cycled Li sample FGB scatters slightly more than pristine Li sample FGA, which can be attributed to increased volume fraction of scatterers (eg. pores) , but it could also be due to difference in thicknesses between the two samples. The SANS curves from pristine Li-CNT sample FGC and cycled Li-CNT sample FGD appear same.

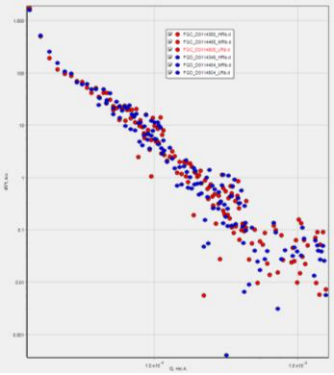

Fig. 2. USANS data of samples FGC, FGD (background subtracted using FG0)

Correlating the structure with Li conductivity in Ga and Al-doped LLZO electrolytes

Neutron Physics Laboratory - Neutron diffraction

Neelima Paul

Proposal ID

542

Proposal ID: #542

Title: Correlating the structure with Li conductivity in Ga and Al-doped LLZO electrolytes

Main proposer: Neelima Paul, TUM Garching, Germany

Instrument & Responsible: MEREDIT, Charles Hervoches

Goal: Both Ga and Al are used as dopants to enhance Li conductivity in LLZO electrolytes. However, it is unclear why Li conductivity is very high in Ga-doped LLZO, whereas it is quite low in Al-doped LLZO. We would like to gain insight on these lithium-ion migration mechanisms by refining the neutron diffraction data to correlate the conductivity with the structure. Additionally, we would like to obtain neutron diffraction data of doped LLZOs after their reaction with Li metal to correlate high Ga conductivity with Li reactivity and ultimately cycling performance of Ga-doped LLZO.

Technical details: We measured four samples for about 1 day each: (1) Li7–3*x*Al*x*La3Zr2O12 powder with x=0.2, (2) Li7–3*x*Ga*x*La3Zr2O12 powder with x=0.2, (3) Li7–3*x*Al*x*La3Zr2O12 pellet with x=0.2 and reacted with Li foil , (4) Li7–3*x*Ga*x*La3Zr2O12 pellet with x=0.2, and reacted with Li foil. The samples were filled in vanadium crucibles just before the measurement and sealed, and thus had a limited air exposure of 1 day (i.e. during measurement).

Results: In general, the statistics are not good, which can be both due to sample and the technique limitations. Rietveld refinements are used to identify the space group and extract lattice parameters for each sample. Al doped LLZO is seen to form a single garnet phase with SG cubic Ia_3d, whereas Ga doped LLZO is seen to form a single garnet phase with SG cubic I_43d with our sample composition. After exposure to air, Li – H exchange can cause slight increase of lattice parameters and appearance of shoulders on lower angle of Bragg peaks. LiCO3 formation can also cause an impurity peak. The Al doped LLZO seems not to change much after Li treatment whereas Ga doped LLZO undergoes a structural transformation to form a single garnet phase SG tetragonal I41/acd after Li treatment. A diffractogram from this sample (and the corresponding fit) is shown in Fig. 1.

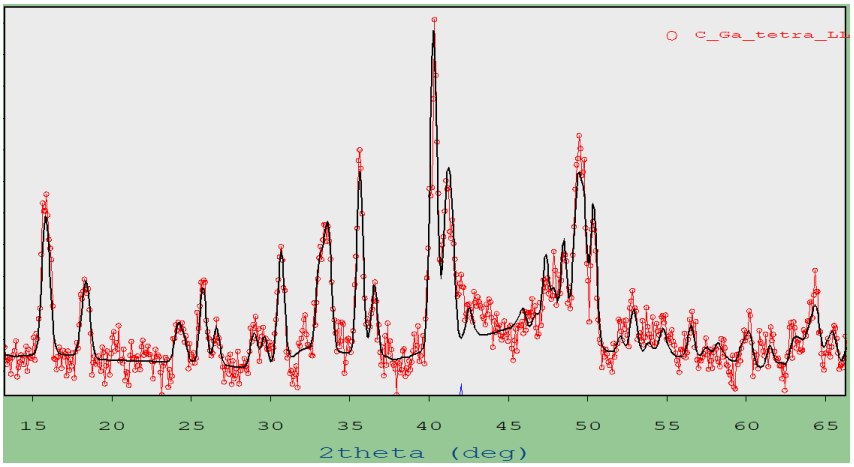

Fig. 1: Neutron diffractogram over a selected angular range for sample 4 (Li treated Ga doped LLZO).

Use of Polycarbonate for radiochromic dosimetry of proton and deuteron beams

Laboratory of Cyclotron and Fast Neutron Generators

David Zoul

Proposal ID

543

Research report

From 29.11.2021 to 30.11.2021, a series of experimental irradiations of radiochromic integrating MAKROCLEAR dosimeters by proton and deuteron beams accelerated on a U-120M cyclotron was performed at the CANAM workplace.

These dosimeters have been developed in the CVŘ since 2016. It is a solid-state clear polymeric material that responds to irradiation by changes in its optical density. For small doses, these changes first occur in the near UV region of the spectrum, then propagate into the light region and for even higher doses pass into the infrared region of the spectrum.

Dosimeters prepared in the shape of blocks measuring 10 x 10 x 20 mm were placed with their longest dimension parallel to the axis of the hadron beam in a special aluminum holder, behind a 10 mm thick aluminum collimator and a 9 mm diameter aperture so that the proton beam axis passes through the center of the sample.

During irradiation, the hadron beam was simultaneously monitored by a Farmer ionization chamber connected to a UNIDOS electrometer calibrated in the absorbed dose, so that the absorbed dose in the sample could be read in real time. The samples were successively irradiated with 15.5 MeV and 34 MeV protons at doses of 500 Gy, 2,500 Gy, 5,000 Gy, 10,000 Gy, 15,000 Gy. The next day, irradiation with 17 MeV deuterons continued at doses of 5,000 Gy, 10,000 Gy, 15,000 Gy.

This was followed by scanning the irradiated dosimeters on an Epson Perfection 850-Pro transmission scanner, through a series of color filters transmitting light wavelengths 640 nm, 580 nm, 510 nm, 450 nm, and through white light with a mean wavelength of 550 nm. The scanning was performed perpendicular to the beam axis to obtain information about the beam dose profile, and along the beam axis to obtain information about the depth dose curve (so-called Bragg curve) of the respective type of radiation. Because the material of dosimeter has only an 8% higher density than the average density of the human body, the results obtained can also be applied to Bragg curves in hadronic therapy of oncological diseases.

The bitmaps obtained by scanning were subsequently freed of noise caused by microscopic dust particles and impurities, which, despite thorough cleaning, were able to adhere to the surface of the samples. Low-pass filter convolution (image integration) was used for this. The convolution kernel consisted of a 3 x 3 matrix.

By accurately measuring the size of each sample with a micrometer gauge and comparing it with the number of pixels, the size of one pixel was determined and thus the correct dimensional scale of individual elements in the image. This made it possible to easily construct graphs of the depth dose curves and dose profiles of the individual bundles used, in a dimensional scale corresponding to reality.

Optical density (vertical axis in the graphs) was determined as absorbance, ie the decimal logarithm of the ratio of the intensity of radiation incident on the sample (mean value of light intensity outside the sample area) and intensity of radiation transmitted by the sample, divided by the thickness of the darkkening area of samples exposed and scanned in different ways).

The results of analyzes performed so far only in white (polychromatic) light have shown that MAKROCLEAR dosimeters are excellent as cheap and easily available integrating dosimeters of protons and light nucleuses in the dose range up to about 10 kGy, where their response in white light is practically linear to dose (with detectability threshold of about 100 Gy). This is approximately 20 times less than was previously observed with the same dosimeters after exposure to gamma photons of cobalt 60. However, this corresponds to the LET ratio for the photons and protons of the energies used, indicating that MACROCLEAR dosimeters respond to the relative biological efficiency (RBE) of different types of radiation, not just the absorbed dose. The MAKROCLEAR dosimeters so directly measure an dose equivalent.

Influence of the forging process on the precipitation behavior in the nickel-based superalloys

Neutron Physics Laboratory - Neutron diffraction

Frank Kümmel

Proposal ID

545

Experimental Report: "Influence of the forging process on the precipitation behaviour in nickel-based superalloys"

F. Kümmel[1], M. Fritton[1], R. Gilles[1]
1) Technical University Munich, Heinz Maier-Leibnitz Zentrum

The evolution of the different phases with temperature and the microstructure after different heat treatments was already investigated for the newly developed VDM® Alloy 780 by the authors of this proposal applying neutron diffraction (ND) and scanning electron microscopy (SEM).[1,2] However, the influence of forging on the precipitation of γ´ remains elusive. To elucidate the effect of forging fully solutionized (1020°C / 1h / air-cooled + 1080°C / 1h / water quenched) VDM® Alloy 780 samples were prepared as follows:

1) + 1000 °C / 1.3h without or with 50% compression / furnace cooling 25 °C/min -> forging

2) + 975 °C / 6h / water quenched -> HT precipitation

3) +800 °C / 6h / air-cooled -> γ´ precipitation

This three-stage processing route mimics the final steps of industrial material processing, i.e. forging (1), HT phase precipitation (2) and hardening phase precipitation (3). To isolate the influence of the forging, each sample was additionally prepared identically without deformation. XRD and SEM investigations were already performed but these techniques probe the alloy locally, leading to limited particle statistics. Therefore ND experiments were performed using the MEREDIT instrument with identical samples to get real bulk information. First results are are shown in Fig. 1.

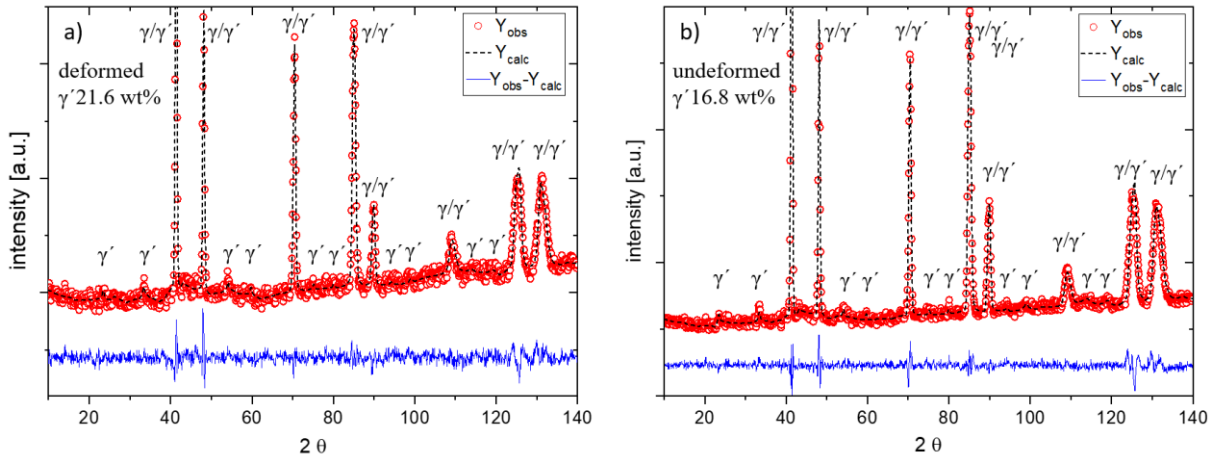

Fig. 1 Rietveld refinements of the VDM® Alloy 780 measured at room temperature (observed data (red circles), calculated data (black dotted line) and difference plot (blue line)) after the complete three-step processing route (1-3) a) for the deformed and b) for the undeformed specimen. The diffractograms were recorded at a wavelength of 1.46 Å.

The Rietveld refinements of condition 3 reveal γ´ phase fractions of 21.6 wt% and 16.8 wt% for the deformed and undeformed samples, respectively. This shows that, as expected, the forging process influences the precipitation process, which is evident from the approximately 5 wt.% higher proportion of γ'-phase in the deformed sample (cf. fig. 1 a).

1) C. Solís et al. in Metall. Mater. Trans. A (2018), 49, 4373–4381.

2) C. Solís et al. in Characterization of Minerals, Metals, and Materials (2019), 23–32

Study of elemental composition of volcanic ashes for geopolymer applications

Laboratory of Tandetron

Giovanni Ceccio

Proposal ID

546

Report - Proposal 546 “Study of elemental composition of volcanic ashes for geopolymer applications”

The project was focused on the determination of elemental composition of several volcanic ashes by nuclear analytical techniques such as RBS and Ion Microprobe-IBA using MeV ions (from Tandetron accelerator).

a) b)

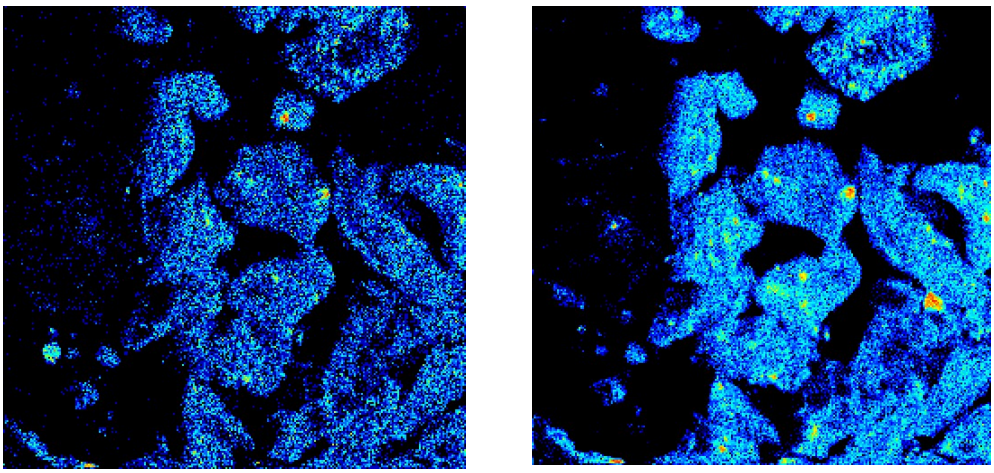

c) d)

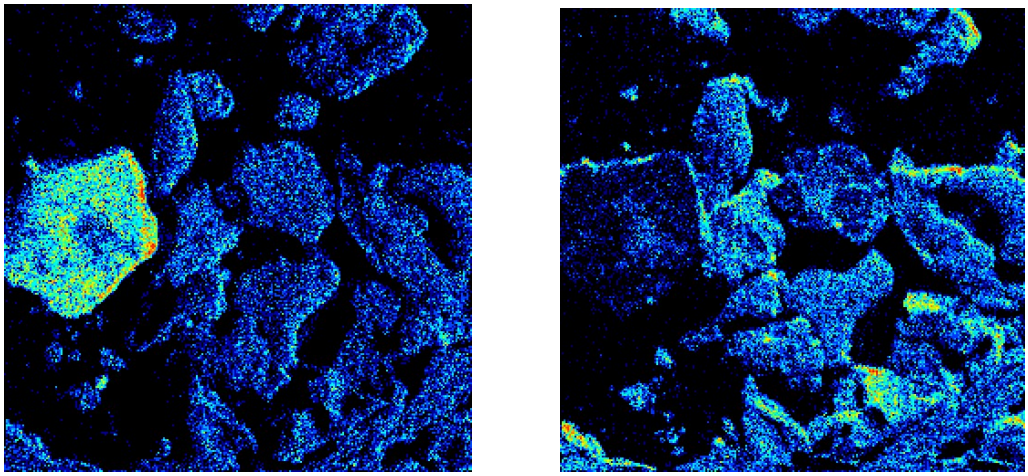

Microbeam analysis of volcano ashes, elemental investigation of: a) Ti, b) Fe, c) Si and d) Al

The obtained data are currently under evaluation and the comparison with complementary techniques suggests the possibility to have small traces of particular elements suitable for the preparation of geopolymers. The results are suitable for future publications when the data evaluation will be completed.

The modification of YSZ implanted with Au using high-energetic oxygen ion irradiation

Laboratory of Tandetron

Romana Mikšová

Proposal ID

486

Report regarding proposal "The modification of YSZ implanted with Au using high-energetic ion irradiation"

Romana Mikšová[1], *Jakub* Cajzl[3], and *Anna* Macková[1,2]
[1]Nuclear Physics Institute of the Czech Academy of Sciences, p.r.i, 250 68 Řež, Czech Republic
[2]Department of Physics, Faculty of Science, J.E. Purkyně University, Pasteurova 3544/1, 400 96 Ústí nad Labem, Czech Republic
[3]Department of Inorganic Chemistry, University of Chemistry and Technology in Prague, 166 28 Prague, Czech Republic

(100)-oriented YSZ crystals were implanted with 1 MeV Au^+ ions at ion fluences of 1.5×10^{16} cm^{-2}, 5.0×10^{16} cm^{-2} and 7.5×10^{16} cm^{-2} and subsequently annealed at 1100 °C in the air for 1 hour. The Si-ion irradiation with energy 10 MeV was used to modify the created Au NPs. The RBS-C spectra (Figure (a) and (b)) showed higher damage in Zr-sublattice up to the projected range of Au ions in YSZ after the ion implantation. Subsequent annealing caused only partial healing of the crystalline YSZ structure, especially in the surface region and two lower ion fluences. 10 MeV Si-ion irradiation increased the disorder in the surface damage region, no additional disorder was observed in the deeper damage region.

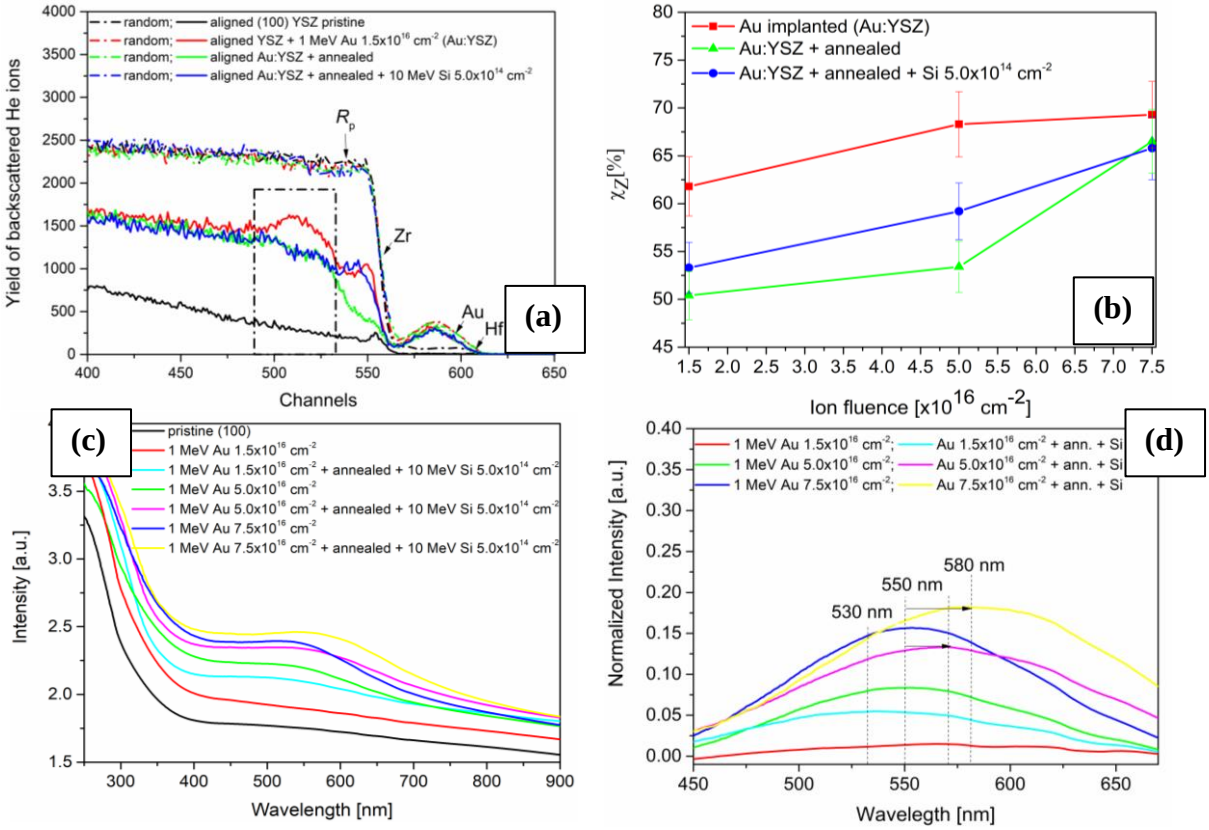

The optical measurement showed the presence of Au NPs. Their growth was more pronounced for the two higher Au-ion fluences, where SPR peaks at 550 nm were shown (Figure (c)). The band was previously connected with two defect types: oxygen vacancies with trapped electrons (F-type centres) nearest to Zr^{4+} cations and hole trapped oxygen ions (V-type centres) adjacent to Y^{3+} cations. After annealing and Si-ion irradiation, the shift of SPR to higher wavelengths (~580 nm) was observed for the two higher ion fluences. It was connected to Au NPs clustering or increasing the size of NPs. For the lowest ion fluence, the SPR peak was observed at ~530 nm (Figure (d) – turquoise line), which correspond to Au NPs formation after annealing.

The part of the results was presented at Applied Nuclear Physics Conference 2021 and published in EPJ proceedings. The next publication will be published in Vacuum in the middle of 2022.

Study of neutron generation inside target made from lead spheres

Laboratory of Cyclotron and Fast Neutron Generators

Ondej Šastný

Proposal ID

487

Final report for experiment

Study of neutron generation inside target made from lead spheres

Ondřej Šťastný, Brno University of Technology

This experiment was aimed to study spatial and energy distribution of neutrons generated inside target made from small lead spheres. This research was focused on advanced spallation target design. It was planned to perform comparison of experimental data and results of simulations using various codes and libraries.

Unfortunately, due to COVID-19 pandemic and resulting restrictions together with several technological challenges, it was decided to postpone this experiment. Especially, the cooling of target must be considered carefully since the lead spheres would easily melt during irradiation phase.

I would like to express my acknowledgment to the Laboratory of Cyclotron and Fast Neutron Generators' staff, especially to Messrs. Jan Štursa and Václav Zach for their assistance, valuable comments, and cooperation.

Neutron depth profiling for understanding the impact of Li-excess in Ni-rich layered NMC cathodes fo

Neutron Physics Laboratory - Nuclear analytical methods with neutrons

Pham Thien An

Proposal ID

551

Report regarding: “Neutron depth profiling for understanding the impact of Li-excess in Ni-rich layered NMC cathodes for long-term battery operation”

THIEN AN PHAM[1,2], AHMAD OMAR [3], DARIA MIKHAILOVA[3], VACÍK JIŘÍ[4], RALPH GILLES[1]

[1]Heinz Maier-Leibnitz Zentrum (MLZ), TU München, Lichtenbergstr. 1, 85748 Garching, Germany
[2]TU München, Physik-Department, LS Funktionelle Materialien, James-Franck-Str. 1, 85748 Garching, Germany
[3]Leibniz Institute for Solid State and Materials Research Dresden, Helmholtzstraße 20, 01069 Dresden, Germany
[4]Nuclear Physics Institute of the Czech Academy of Sciences, Husinec - Řež, čp. 130, 250 68 Řež, Czech Republic

Ni-rich electrode materials should have been investigated using the neutron depth profiling method. For that, samples of different compositions in pristine state and after ten charge-discharge cycles were prepared. The samples were sealed in kapton foil to prevent degradation as the Li is very reactive, and the composition of the samples could change when in contact with ambient air. Unfortunately, the thickness of the used foils was too high; therefore, the signal from the samples was too low to retrieve more information.

Figure 1 shows the difference between a pristine sample and one cycled for ten cycles. Here, the difference between the counts per second was minuscule despite the long measuring time, which can be attributed to the absorption of the kapton foil.

Unfortunately, the measurements were conducted right at the end of the project period, and thus, there were no remaining funds to start another campaign to prepare a new batch of samples. Therefore, this measurement was stopped.

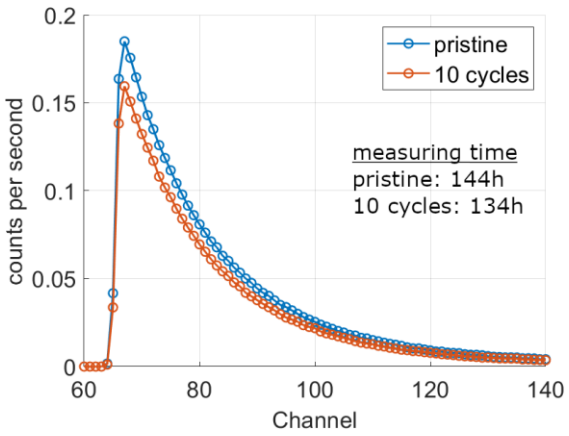

Figure 1: NDP spectra for a pristine and a cylced electrode.

Ionizing radiation on Mars: experimental activities in support of ExoMars space mission

Laboratory of Tandetron

John Robert Brucato

Proposal ID

553

Report of experimental activities in support of ExoMars space mission

John Robert Brucato
INAF-Astrophysical Observatory of Arcetri, L.go E. Fermi 5, 50125 Firenze, Italy

At Tandetron we made the first set of irradiations with with H and He ions of multiple samples simultaneously. We have prepared 26 samples of hydrated silicate vermiculite $(Mg, Fe, Al)_3 (Al, Si)_4O_{10} (OH)_2 \times 4(H_2O)$ mixed with two biomolecules L-phenylalanine and undecanoic acid at 10% concentration. Specifically, 12 samples of vermiculite + L-phenylalanine, 12 samples of vermiculite + undecanoic acid and 2 blank samples of pure vermiculite were prepared and irradiated.

Figure 1 reports the CAD drawing of the sample container. It has a cylindrical symmetry with a major diameter of 2.0 cm and a total height, after removing the protective top lid, of 1.2 cm. The inner volume can host a sample in the form of a cylindrical pellet. The sample container is AISI 304 stainless steel.

Once the vermiculite sample + molecule was prepared it was pressed into the sample holder at 2 ton pressing, pellets with masses of about 0.67 g, diameter of 1 cm and thickness of 4.65 mm were obtained. Since vermiculite has an average bulk density of 2.5 g / cm^3, the average density of the pellets obtained by pressing vermiculite into the sample container were 1.67 g / cm^3.

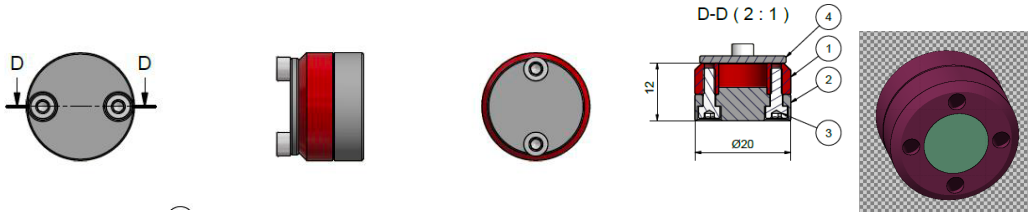

Figure 1. Sample container made of AISI 304 stainless steel. The protons and Helium ions impinged on the exposed surface once the top protective lid was removed.

The samples were irradiated at Tandetron during the period 14-16 March 2022 with:

1) H+ 5 MeV with total fluence between 10^{14} and 10^{15} H^+ / cm^2
2) He+ 9 MeV with fluence between 10^{13} and 10^{14} He^+ / cm^2

The total ionizing dose for H+ and He+ particles was estimated of about 10 kGy and and 600 kGy , respectively. Simulation showed that the first millimeter depth of the samples is affected by the total ionizing dose. The analysis of the irradiated samples stared and is in progress. Samples were characterized with infrared spectroscopy.

Micro infrared mapping measurements are reported in Figure 2. Top right panel shows the picture of vermiculite + undecanoic acid after it was exposed to proton irradiation. Colored dots represent the spots where micro-IR spactra where acquired. The spectra are reported in the bottom panel. The top left panel shows the spectral intensity distribution along the surface sample. First results showed a degradation pattern of the biomolecules according to the total ionizing dose of H+ and He+ ions. The cross section of degradation will be evaluated and extrapolated to the lifetime on Martian conditions.

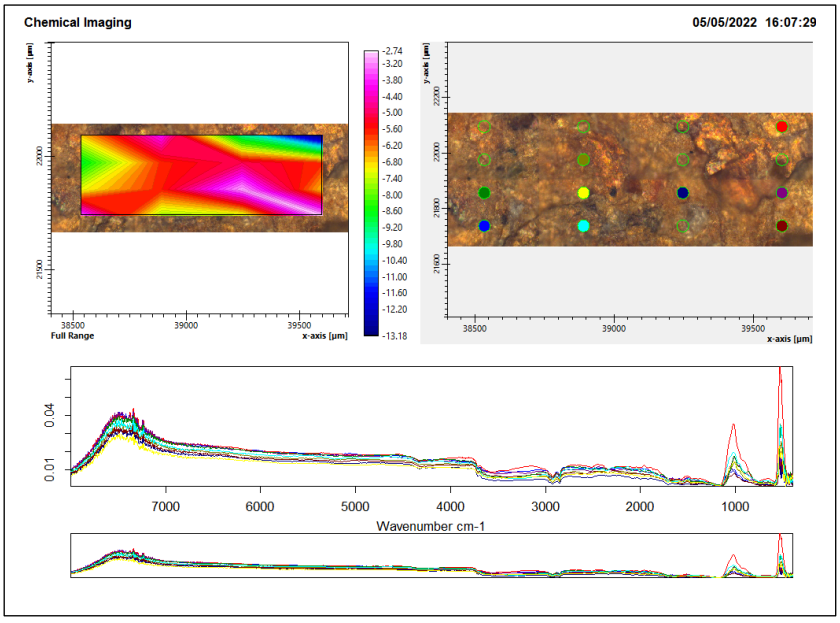

Nanostructuring of crystalline ZnO by energetic ion beams for optoelectronic applications

Laboratory of Tandetron

Adela Jagerova

Proposal ID

490

Report regarding proposal "Nanostructuring of crystalline ZnO by energetic ion beams for optoelectronic applications"

Adéla Jagerová[1,2], *Jan* Mistrík[3,4], and *Anna* Macková[1,2]
[1]Nuclear Physics Institute of the Czech Academy of Sciences, p.r.i, 250 68 Řež, Czech Republic
[2]Department of Physics, Faculty of Science, J.E. Purkyně University, Pasteurova 3544/1, 400 96 Ústí nad Labem, Czech Republic
[3]Institute of Applied Physics and Mathematics, Faculty of Chemical Technology, University of Pardubice, 532 10 Pardubice, Czech Republic
[4]Centre of Materials and Nanotechnologies, Faculty of Chemical Technology, University of Pardubice, 530 02 Pardubice, Czech Republic

The surfaces of *c*-, *a*- and *m-plane* ZnO were nano-structured using the 27 MeV W ion irradiation with ion fluences of 5×10^{9}, 5×10^{10} and 5×10^{11} cm^{-2}. RBS-C analysis revealed only low Zn-disorder up to the depth of 1.38 μm in all studied orientations (e.g. Figure 1a for *c-plane* ZnO). The irradiation-induced increase of surface roughness and formation of nano-hillocks on the *c*- and *a-plane* ZnO and huge moulds on the *m-plane* ZnO (Figure 1b and c for *c*- and *m-plane* ZnO, respectively).

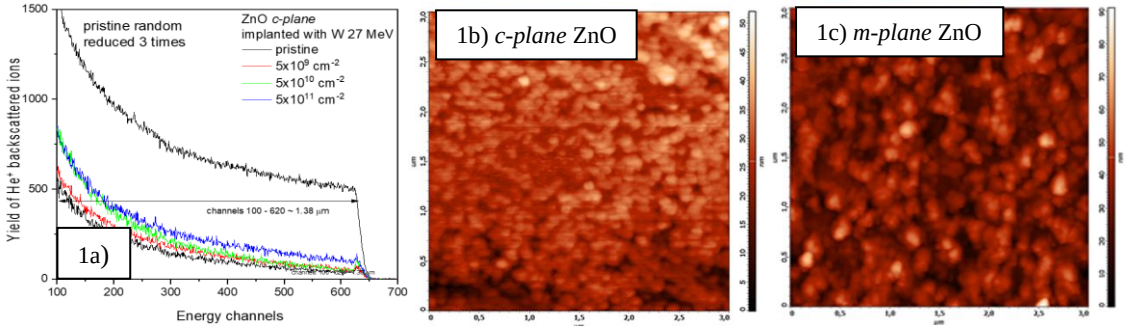

The crystalline ZnO nanopillars with a thickness of about 400 nm were modified with Au NPs prepared by 400 keV Au ion implantation with ion fluences of 1×10^{15}, 5×10^{15} and 1×10^{16} cm^{-2}. The growth of Au NPs was further supported with thermal annealing at 600 °C on air. The ion implantation decreases ZnO nanopillar thickness as observed by RBS (Figure 2a). The implanted Au ions modified the depth of about 250 nm. The higher implantation depth exhibited a shift of implanted Au ions towards the surface, see Figure 2b. The distribution of implanted Au ions did not significantly change after thermal annealing. The optical properties of implanted ZnO nanopillars, expressed by extinction coefficient, showed surfaced plasmon resonance (SPR) peak typical for Au NPs in a wavelength region of 400 – 800 nm, see Figure 2c. The SPR peak is shifted against a higher wavelength with increasing Au ion fluence indicating the creation of bigger Au NPs with higher fluence. SPR peak is further shifted towards a higher wavelength after thermal annealing due to the growth of Au NPs and the formation of bigger complex clusters.

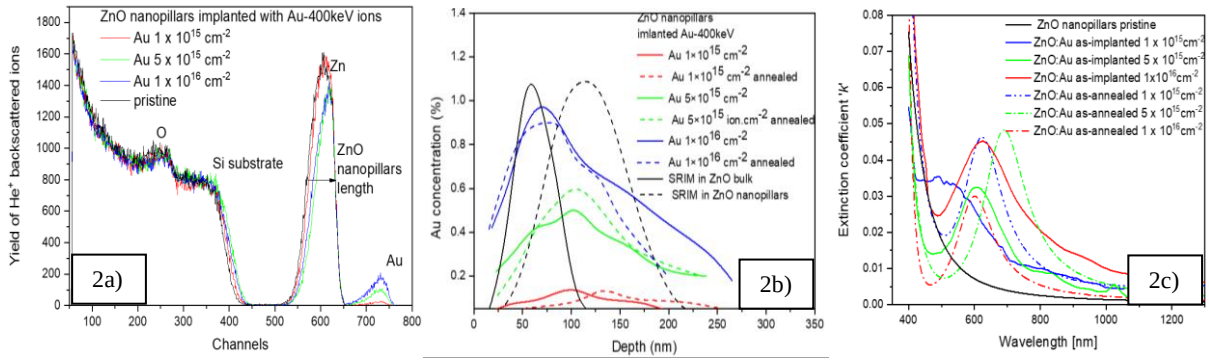

The results obtained for 27 MeV W irradiated *c*-, *a*- and *m-plane* ZnO surfaces were summarized and published in Physical Chemistry Chemical Physics journal. The modification of ZnO nanopillars with Au NPs prepared with 400 keV Au implantation was published in the Journal of Physics D: Applied Physics.

Localisation of the stresses in Mg alloy during compression test - part 1

Neutron Physics Laboratory - Neutron diffraction

Andrzej Baczmanski

Proposal ID

556

Report regarding proposal: "Localisation of the stresses in Mg alloy during compression test - part 1"

Andrzej Baczmański, Marcin Wroński, Przemysław Kot and Sebastian Wroński, AGH- University of Science and Technology, al. Mickiewicza 30, 30-059 Krakow, Poland

The aim of the experiment was to investigate the evolution of resolved stresses on slip and twining systems and stresses localised at chosen grains in textured AZ31 magnesium alloy (pole figure is shown in Fig. 1 a). The neutron diffraction method was applied during *in-situ* compression tests along RD (rolling direction), ND (normal direction) and direction tilted by 30˚ from ND direction (cf. stress-strain curves shown in Fig. 1 b), in order to activate different sets of slip and twinning mechanisms. The lattice strains were measured for selected different *hkl* reflections and orientations of the scattering (using the Eulerian cradle) corresponding to chosen groups of grains, as shown in Fig. 1 a [1].

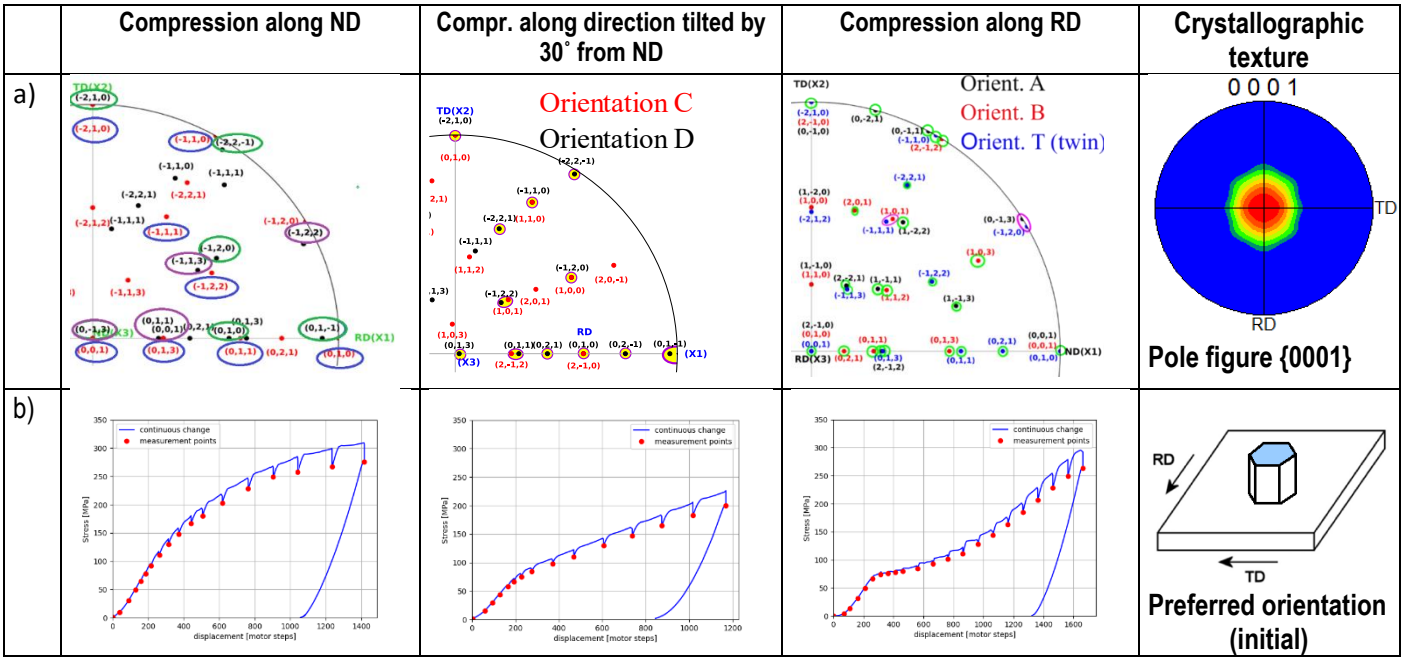

Fig.1. a) Poles for which the lattice strains were measured during *in situ* compression along: RD, direction tilted by 30˚ from ND and ND; pole figure {0001} and preferred texture orientation; b) macroscopic stress-strain plots for three compression tests with marked measurement points.

The crystallite group method [1] was applied to determine the stresses localised at grains (having preferred texture orientations) from the measured *in situ* lattice strains. Then, the evolution of resolved shear stresses (RSS) for the selected slip systems and twinning system were determined and the critical resolved stresses (CRSS) were found analysing changes in the trends of *CRSS vs. macrostress* plots, shown in Fig. 2. The CRSS values estimated in this experiment (basal slip, pyramidal slip and twinning systems) are given in Fig. 2, while the CRSS value of 68 MPa for the prismatic slip system $\{1\bar{1}00\}\langle 11\bar{2}0\rangle$ was determined in the previous experiment performed at TKSN-400 (NPI, Řež) [1].

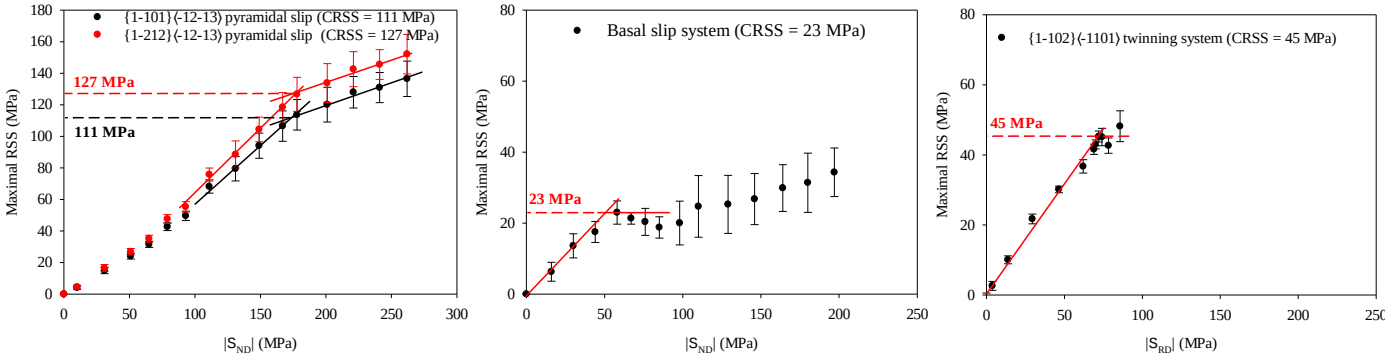

Fig.2. Dependence of maximum resolved shear stress (RSS) in function of macrostress. The CRSS values are determined analysing the changes in the trends of the plots.

Conclusions:

- Different elastoplastic behaviours in different macroscopic directions were observed for textured AZ31 magnesium alloy.
- Stresses localized at grains having preferred texture orientations, values of RSS and CRSS for slip and twinning systems were determined using crystallite group method for the *in-situ* neutron diffraction measurement during compression/tensile test.
- The results obtained in current experiment agree and support results obtained previously for the same material using TOF diffraction (EPSILON diffractometer) in JINR in Dubna [2].

References:

[1] A. Baczmański, P. Kot, et al. Materials Science and Engineering A. 801 (2021) 140400.
[2] Przemysław Kot, "Diffraction study of deformation process for selected groups of grains and different phases in polycrystalline materials", PhD Thesis, defence planned 7.11.2022 at AGH, Kraków

Effect of Drying, Calendering, and Plating on Silicon-dominated anodes for Lithium ion batteries

Neutron Physics Laboratory - Nuclear analytical methods with neutrons

Lukas Grossmann

Proposal ID

559

Introduction

Anodes containing silicon as active material are promising candidates for future Lithium Ion Batteries (LIB) due to the tenfold electrochemical capacity of Si compared to commonly used graphite. However, the extreme volume expansion of Si upon lithiation of up to ~300% leads to continuous degradation of Si-dominated anodes upon cycling. The reason for that is the electrochemical milling of Si particles followed by ongoing formation of new Solid-Electrolyte-Interface (SEI) layers on electrolyte-exposed Si surfaces which consumes active Si in the cell.[1]
We use a novel material concept of anodes with micrometer-sized Si particles as active material which are lithiated only partially to 30% (1200 mAh/g(Si)).[2] This strongly mitigates the unwanted effects and still accounts to a three times higher capacity as compared to common graphite. Up to now, this approach yielded an increased cycling stability by approximately one order of magnitude (~40 cycles against ~200 cycles).
With our proposed experiments we want to investigate the Li-distribution inside the anodes as a function of important parameters. Overall, three parameters are to be surveyed by Neutron Depth Profiling (NDP) to get a better understanding of the capabilities and limits of our material concept.
The anode mixture consists of 70 wt.% Si, 20 wt.% graphite, and 10 wt.% Li-containing poly-acrylate binder (LiPAA). It is well-known from literature that the binder distribution is important for mechanical integrity of the coating and potentially also the electrochemical performance.[3] In this regard, we propose NDP to be a fast and reliable method to analyze the homogeneity of the LiPAA binder across the electrode, which would extend the capabilities of this method toward LIB production.
A second crucial step in anode production is the calendaring process. Thereby, the porosity of the coating is reduced which normally leads to a lower rate capability, yet increases the volumetric energy density of the material. However, the reduced rate capability leads to overpotentials at high lithiation rates which are assumed to cause a Li gradient inside the electrode, where the material near the surface is more lithiated than the interface to the collector.
The third aspect to be studied is the Li plating phenomenon in our anodes. Li plating was identified to be a crucial safety aspect in modern LIB.[4] Due to the higher potential of Si with 0.4 V against Li/Li^+ as compared to graphite with 0.05 V, Li-plating should be less probable. However, for very high lithiation rates, the overpotentials can increase in such a way that Li-plating becomes feasible. We suggest NDP as reliable method to observe traces of Li-plating in samples lithiated at very high rates with huge overpotentials.
Note, that our previous NDP experiments proved that NDP is suitable for studying Si-related anodes, especially Si-graphite composites.[5-7]

Experimental

The experiments encompass six samples of the Si-dominated anode mixture coated on the Cu collector. Samples (1) and (2) are meant to explore the binder distribution inside the coating as a function of the drying temperature. For sample (1) the coating procedure was performed at room temperature, while for sample (2) the Cu collector was preheated to 80°C to simulate a fast drying process. Since the LiPAA binder is the only Li containing material in these samples, the Li depth distribution will be directly correlated to the binder distribution. In contrast to samples (1) and (2), the following anode samples are extracted from cells (coin cell format) after various electrochemical treatments.
With samples (3) and (4) we want to investigate the rate capabilities of samples calendered to a porosity of ~30%. At high rates of 1.5 C with a voltage cutoff at 0 V vs Li/Li^+, we observe a high electrochemical overpotential in the anode, which may lead to further lithiation of unused Si particles. We expect that these overpotentials should cause an increased lithiation of near-surface particles, due to the reduced Li^+ mobility throughout the low-porosity samples.
Samples (5) and (6) will be used to study the Li-plating mechanism in our new anode concept. The anodes were lithiated at high rates of 1.5 C with a capacity limit of 1200 mAh/g(Si) and a negative potential against a Li/Li^+ reference electrode was observed, which could lead to precipitation of Li metal on the anode surface. This would result in a distinctive signal in the Li depth profile as measured by NDP.
In all of these samples the Li concentration as a function of depth will be measured by NDP, covered with Kapton foil (thickness ~7.5 µm) to suppress alpha particles and reduce the incoming signal only to the detection of tritons. Every sample will be stored inside an impermeable argon-filled pouch-cell bag since the lithiated Si exhibits fast degradation when exposed to air. This bag will have an implemented Kapton window through which the NDP measurement can be performed. Additionally, all samples will be delivered packed in a large protective bag. For NDP analysis, the samples will be mounted onto the sample holder and transferred into the vacuum chamber. A fast procedure will prevent unnecessary degradation of the samples prior to measurement. The Si-dominated anodes will be measured on their front side, i.e. the neutron beam will directly illuminate the coated side of the electrode.
We expect to measure two samples per day, as we need good statistics across the entire electrode thickness. In total, we ask for three days of beamtime.

References

[1] Gonzalez, Joseph, et al. Journal of Power Sources 269 (2014): 334-343.
[2] Jantke, Dominik, et al. Journal of The Electrochemical Society 166.16 (2019): A3881.
[3] Westphal, Bastian, et al. ECS Transactions 64.22 (2015): 57.
[4] Waldmann, Thomas, Björn-Ingo Hogg, and Margret Wohlfahrt-Mehrens. Journal of Power Sources 384 (2018): 107-124.
[5] Wetjen, Morten, Gilles, Ralph et al. Journal of The Electrochemical Society 165.10 (2018): A2340.
[6] Wetjen, Morten, Gilles, Ralph et al. Journal of The Electrochemical Society 166.8 (2019): A1408.
[7] Moyassari, Erfan, Gilles, Ralph et al. Journal of The Electrochemical Society 168.2 (2021): 020519.

Crystal structure studying of the Mn55Al45C2T (T= Mo, Cr, Cu, MoC) alloys

Neutron Physics Laboratory - Neutron diffraction

Vitalii Shtender

Proposal ID

496

Report regarding proposal "Crystal structure studying of the $Mn_{55}Al_{45}C_2T$ (T= Mo, Cr) alloys"

V. Shtender, M. Sahlberg, Uppsala University, Sweden
C. Hervoches P. Beran, Nucl. Physics Inst., Rez, Czech Republic

The goal was to prepare $Mn_{55}Al_{45}C_2$ with well dispersed nanoparticles or carbide former to create pinning sites. For this, we therefore intentionally added different amount of carbides, nitrides and oxides or simple d-metals to the $Mn_{55}Al_{45}C_2$ to elucidate their effect on the microstructure and magnetic properties. Fig. 1a shows XRD pattern for $Mn_{55}Al_{45}C_2Mo_2$ where some over intensities are observed which could relate to the influence of Mo on the structural feature (preffered orientation has been taken into account). As can be seen in Fig. 1b homogeneous distribution of the Mo in alloy matrix has been distinguished (τ /ε phase ration will be improved with annealing). In this proposal we wanted to investigate $Mn_{55}Al_{45}C_2T$ (T= Mo, Cr, Cu and MoC) alloys and find out influence of the dopants on the τ-phase.

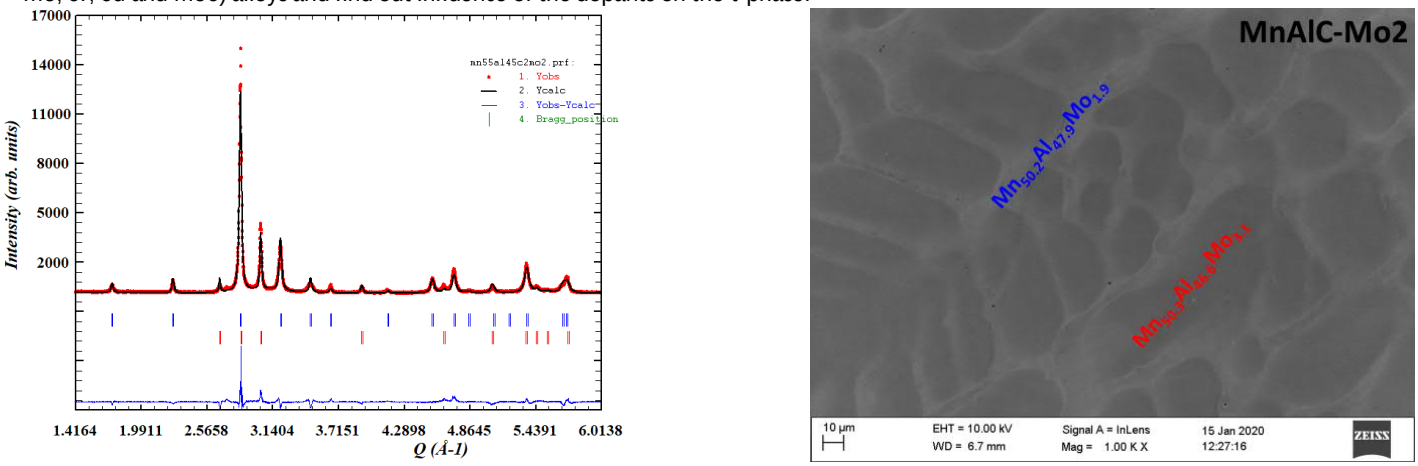

a) *b)*

Figure 1 a) refined XRD of $Mn_{55}Al_{45}C_2Mo_2$ and b) SEM/EDS on the as cast $Mn_{55}Al_{45}C_2Mo_2$ alloy

Neutron powder diffraction experiments were performed on $Mn_{55}Al_{45}C_2Mo_2$ and $Mn_{55}Al_{45}C_2Cr$ at 298 K using the MEREDIT instrument. The motivation for the experiments was to investigate the possible incorporation of the Mo and Cr into the structure of tau-MnAl phase.

The extracted data is still under evaluation but preliminary results propose Mo goes to the structure of tau-phase (the same as it was indicated with SEM/EDS). Observed and calculated neutron powder diffraction profiles are shown in fig. 1. The preliminary proposed magnetic structure which is along the z-axis with a central atom in the opposite direction

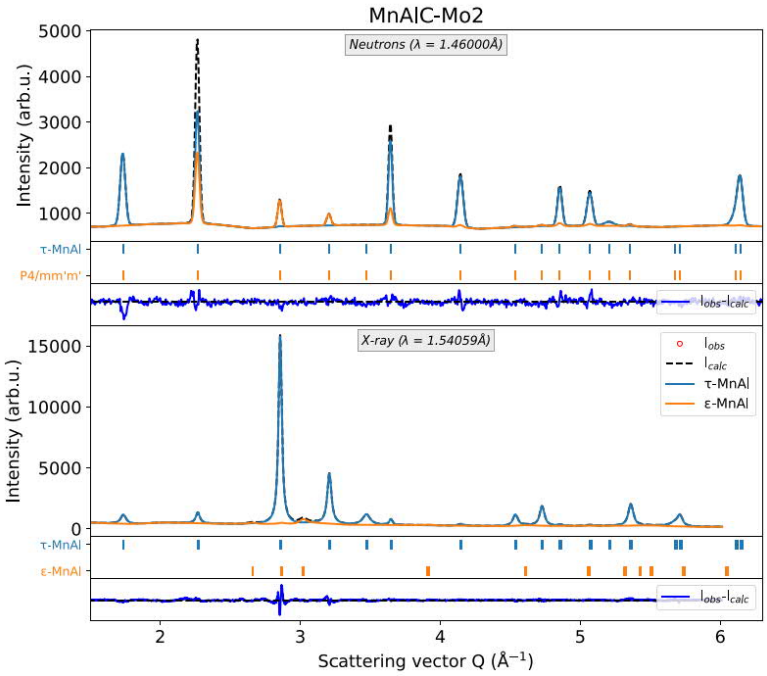

Fig 1. Joint refinement of the XRD and NPD for Mn $Mn_{55}Al_{45}C_2Mo_2$ at 298K.

Characterisation of glass tesserae from unique mediaeval statue of Madonna in Malbork (PL)

Laboratory of Tandetron

Zdeka ermáková

Proposal ID

560

Report regarding proposal “Characterisation of glass tesserae from unique mediaeval statue of Madonna in Malbork (PL)”

Z. Čermáková, S. Švarcová, Institute of Inorganic Chemistry of CAS, v.v.i., Řež, Czech Republic

V. Havránek, Nuclear Physics Insitute of CAS, v.v.i., Řež, Czech Republic

Malbork Madonna is a unique mediaeval statue (destroyed at the end of World War II, but re-erected during recent restoration campaign with newly-made glass tesserae). The subject of this PIXE study were three types of preserved tesserae with special focus on a blue tessera, which was suspected to be original mediaeval. The measurements yielded elemental maps (Fig. 1), however, elements present at low concentration (see Sr) were very difficult to detect, and the obtained results were comparable with maps previously achieved by SEM-EDS.

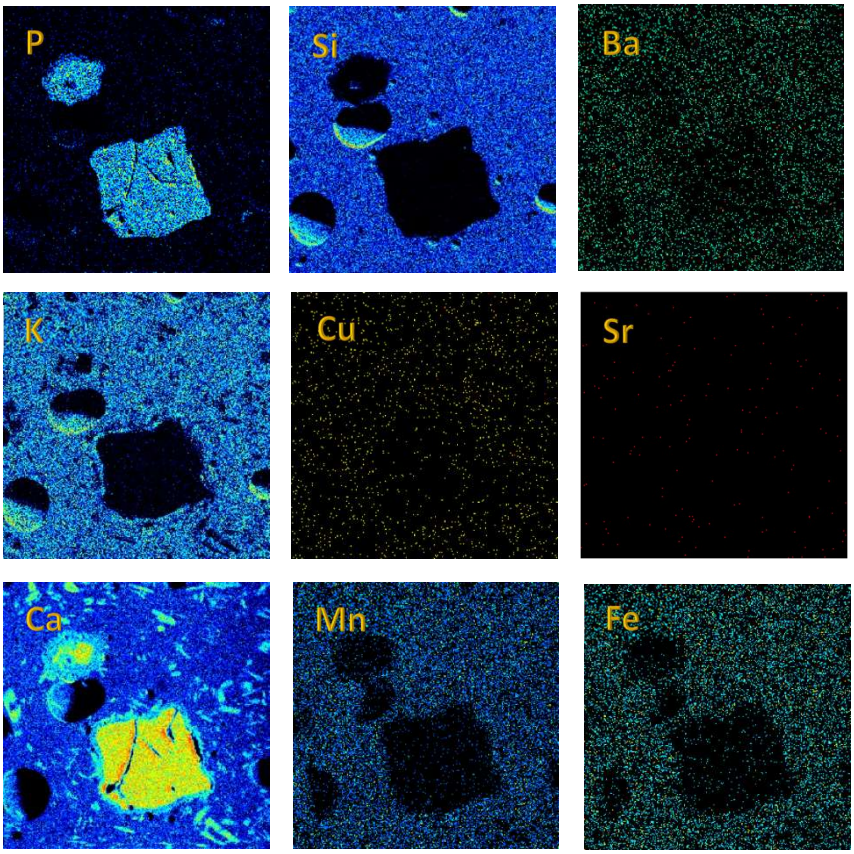

Fig. 1 PIXE elemental maps of the blue Malbork tessera with visible angular grains of Ca-phosphate and smaller inclusions of wollastonite/pseudowollastonite (phases identified by Raman microspectroscopy)

The calculations yielded some interesting results, such as confirmation of presence of Ba, or the detection of Ni, Cu or Zn, however, the analysis (especially if smaller areas were intended for future measurements) does not seem suitable for our purposes and it will be more meaningful to measure the samples by LA-ICP-MS, even though micro-destructive.

Fluoride target matrices for analysis of Ni and Ca isotopes

Laboratory of Tandetron

Tomáš Prášek

Proposal ID

561

Report regarding proposal Fluoride target matrices for analysis of Ni and Ca isotopes

Mass analysis of Ni and Ca fluoride target matrices, aimed mostly for potential application in ^{59}Ni and ^{41}Ca analysis, was performed by means of low energy part of 4130 MC Tandetron beamline. Besides, sputtering behaviour of major ineterferents, i.e. cobalt and potassium, was also investigated. The measurement of the materials was carried out using their mixtures with PbF_2 (1:1 mass ratio) in copper and silver cathodes. using PbF_2 as a source of fluoride ions (mass ratio 1:1). Due to ion source current limitation, the caesium temperature during fluorides sputtering was set to 30 °C along with target voltage ranging from 1,9 to 3 kV.

Mass spectra of the respective samples were analysed, focusing predominantly on identification of the high intensity fluoride ion species. Sample with calcium creates predominantly ions $[CaF]^-$ and $[CaF_3]^-$ while potassium creates mostly $[KF_2]^-$. For this reason, application of $[CaF]^-$ and $[CaF_3]^-$ ions for both analysis and implantations can be considered. For samples containing nickel, the suppression of isobaric interference is significantly lower, with cobalt producing intensive fluoride ions. On the other hand, low intensity of $[CoF_5]^-$ and $[CoF_6]^-$ provides some space for further investigation. In this respect, corresponding nickel ions $[NiF_5]^-$ and $[NiF_6]^-$ production needs to be studied in detail. Besides, using hydrated fluoride compounds as target materials was observed to cause ion source instability and is therefore not recommended. Obtained mass spectra of the calcium and nickel fluorides are listed below.

In future research, application possibility of CaF_2 targets for $[CaF_3]^-$ extraction will be further studied also with MILEA AMS system, while a sufficient suppression of cobalt interference in nickel samples cannot be achieved only by using fluoride target materials and requires additional separation.

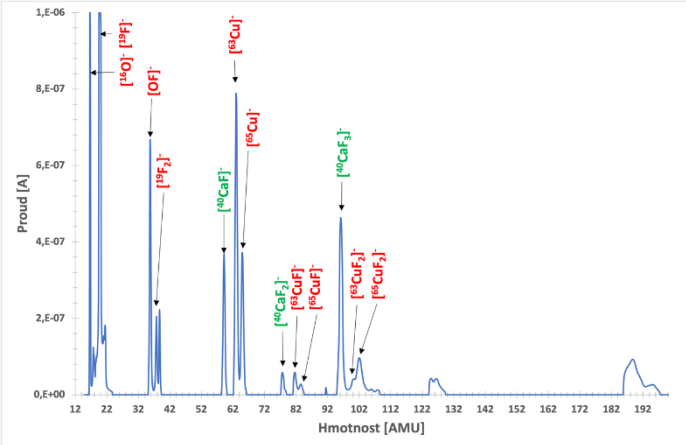

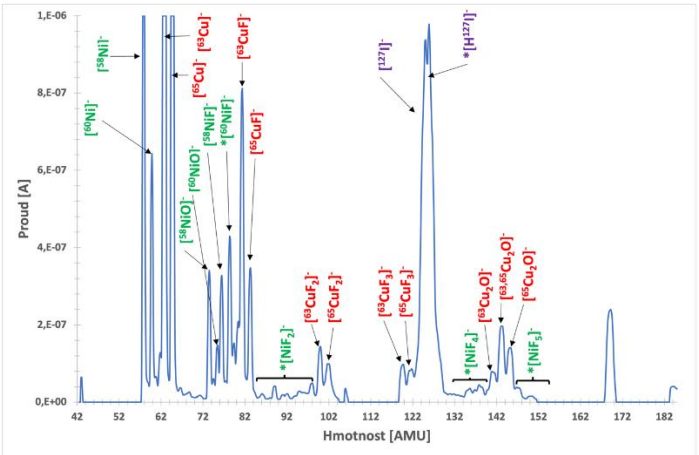

Structural study of the novel superconductor UTe2

Laboratory of Tandetron

Evgenia Chitrova

Proposal ID

565

Structural study of the novel superconductor UTe_2

Evgenia A. Tereshina-Chitrova, O. Koloskova, P. Malinsky, A. Mackova

The recent discovery of unconventional superconductivity in UTe_2 [1] has sparked a keen interest in conducting thorough investigations into compounds with different U to Te ratios. In our work we focused on studying the formation and properties of U-Te thin films with varied composition prepared by the *dc* sputtering technique.

Measurement of Te/U layers was carried out at the ÚJF of the Academy of Sciences of the Czech Republic on a Tandetron 4130 MC tandem accelerator. The samples were measured by the RBS method using a beam of He+ ions with energies of 1.7 and 2.5 MeV to determine the concentration of U and Te on a straight geometry (entry angle 0°, scattering angle 170°) and on an oblique geometry (entry angle 50°, scattering angle 170°). The RBS-Ch method was used to determine single crystal quality, where appropriate. The spectra were evaluated with the software SIMNRA 6.06.

First of all, the RBS study showed that MgO substrates are not appropriate for the samples production at elevated temperatures as both Mg and O diffuse into the thickness of the film. Hence, for the samples production on MgO substrates (very close lattice parameter in MgO with lattice parameter *b* in UTe_2), the substrates have to be cooled to avoid interdiffusion. Second problem revealed by RBS is that thermal sputtering of Te is not suitable for production of homogeneous samples, as from measuring depth profiles of U, Te, and Mg or F we found the concentration gradient in all the samples.

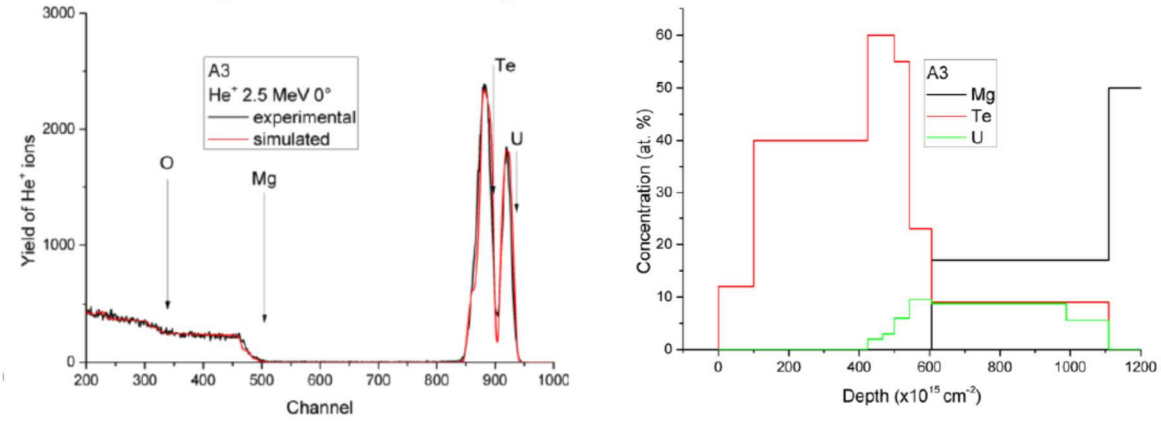

Figure 1: RBS spectra and U and Te depth profiles of sample A3. In addition to U and Te, the presence of other elements (O, C or N) in the layer is assumed, which would had to be verified by further measurements. On the depth profiles of the elements (bottom right) is an obvious surface layer containing Te 0 (400×1015cm-2) and only below it begins a layer containing both Te and U.

Solution for this problem is in constructing a special shape of the sputter source, where uranium and Te first sputter into some (closed) volume and then are released onto the substrate in a controllable manner. We have already prepared a new set of samples, which will be further investigated in our next proposal.

References:

[1] S. Ran et al., Science 365, 684 (2019).

Micro and nano-sized membranes on polyethylene terephthalate realized by ion micro beam

Laboratory of Tandetron

Mariapompea Cutroneo

Proposal ID

568

Report 568

Polymer membranes are conventionally prepared using high-energy particles from radioactive decay or by the bombardment of hundreds of MeVs energy ions. In both circumstances, tracks of damage are produced by particles/ions passing through the polymer, and successively, the damaged material is removed by chemical etching to create narrow pores. This process ensures nanosized pore diameter but with random placement, leading to non-uniform local pore density and low membrane porosity, which is necessary to reduce the risk of their overlapping. The present study is focused on the use of polyethylene terephthalate (PET) foils irradiated by 10.0 MeV carbon ions, easily achievable with ordinary ion accelerators. The ion irradiation conditions and the chemical etching conditions were monitored to obtain customized pore locations without pore overlapping in PET. The quality, shape, and size of the pores generated in the micromembranes can have a large impact on their applicability.

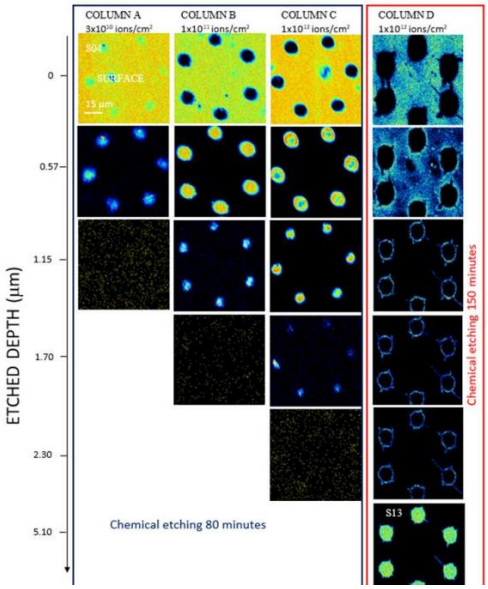

The results indicate that the depth of the pores fabricated on PET foils by ion irradiation progressively increases with the ion fluence and, at the same ion fluence condition, increases with the chemical etching time. **Figure 1** shows the details of the pore edges and the surface morphology of the polymeric foils at 75 μm × 75 μm scan size, considering one pattern as almost representative of the whole membrane.

The Scanning Transmission Ion Microscopy (STIM) coupled with a computer code created in our laboratory was implemented to acquire new visual and quantitative insights on fabricated membranes.

The TrackHH is the code based on the Monte Carlo simulation which is the corrected version of the previous TOM. The modeling of the pore size and shape is obtained through the comparison of the experimental and the simulated energy spectra. The spectra are computed using a very low ion beam divergence and almost 0◦ incidence angle and use the following free parameters: thickness, density, inhomogeneities and structure of the used foil, number of tracks formed in the foil, and pore geometry.

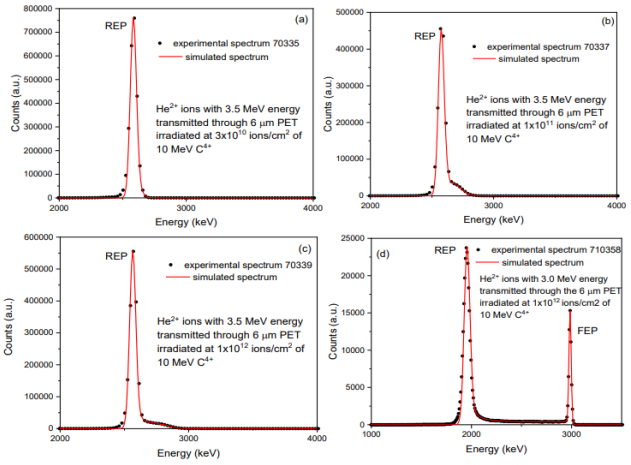

Figure 2. Comparison between the experimental and simulated spectra obtained by TrackHH code for the PET foils irradiated by ions.

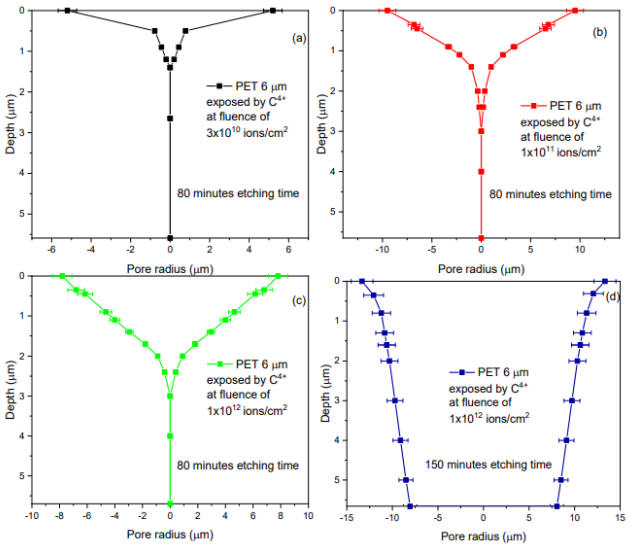

Figure 3. Model of the pores' shape for the membranes

Over the undeniable advantages related to the use of ion lithography processing, the good control of the ion fluence and the high blanking time are crucial for the production of membranes enclosing pores in a chosen pattern. This technique minimizes the merging of the adjacent tracks and promotes the customization of the size and shape of the pores. A Tandetron accelerator, widely available in plenty of laboratories all over the world, was used to deliver carbon ions with an energy of 10 MeV focused by a micro ion beam system on a thin PET foil. The latent tracks formed by ion irradiation of the foils were converted into channels after chemical etching. Conversely, at an ion fluence of 1×10^{12} ions/cm^2 and 150 min etching time, the pores were fully etched and showed a cylindrical shape and diameter of about 20 μm. The joint application of STIM and TrackHH presented congruence in both the formed pore size and the value of the final foil thickness. The relative error in pore size can be estimated at about 10% by direct comparison between the value of the pore diameters evaluated by STIM and TrackHH code.

Ni4(Nb,W,Ti)2O9 corundum like-compounds: cationic distribution and magnetic structure.

Neutron Physics Laboratory - Neutron diffraction

Christine Martin

Proposal ID

569

Report regarding the proposal "$Ni_4(Nb,W,Ti)_2O_9$ corundum like-compounds: cationic distribution and magnetic structure." by C. Martin *et al.*

Neutron powder diffraction was performed using the MEREDIT diffractometer at room temperature, 55 K and 15 K, for two samples corresponding to x = 0.05 and x = 0.1 in the $Ni_4Nb^{5+}_{2-x}Ti^{4+}_xW^{6+}_xO_9$ formula.

The results are described below for the x=0.1 sample.
The RT NPD pattern is characteristic of the expected large *Fdd2* cell (*a* = 28.568 Å, *b* = 10.091Å and *c* = 17.538 Å). A very small amount of NiO is also observed. The refinement of the structure, also using the synchrotron diffraction data obtained in ALBA (Spain), is in progress. Indeed, the calculations are rather delicate since the structure corresponds to 18 oxygen positions, 10 nickel positions and 4 niobium positions, on these 32 sites, only 4 are not general, and mixed occupations have to be introduced to distribute Ti and W (on Nb sites probably). Moreover, some peaks of the SXRPD patterns are broadened compared to the others, probably in link with some disorder due to the mixing of the cations. In addition, transmission electron microscopy is also in progress to confirm (or not) the space group and the metric, to have information on the cationic distribution and on the existence of structural defects.
The *figure 1* shows the beginning of this structural refinement work with the starting patterns (in combined mode, by using Fullprof software).

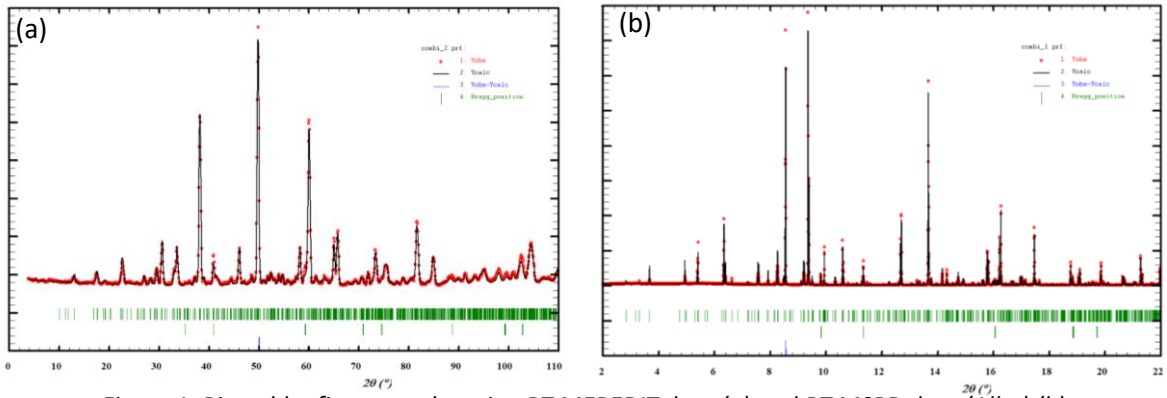

Figure 1: Rietveld refinements by using RT MEREDIT data (a) and RT MSPD data (Alba) (b).

The temperature dependence of the NPD patterns, shown in *figure 2a*, is in agreement with the magnetic properties, illustrated in *figures 2a and b*: magnetic peaks are observed at 55 K and 15 K (highlighted by vertical orange arrows) those relative intensities are varying in between both low temperature patterns.

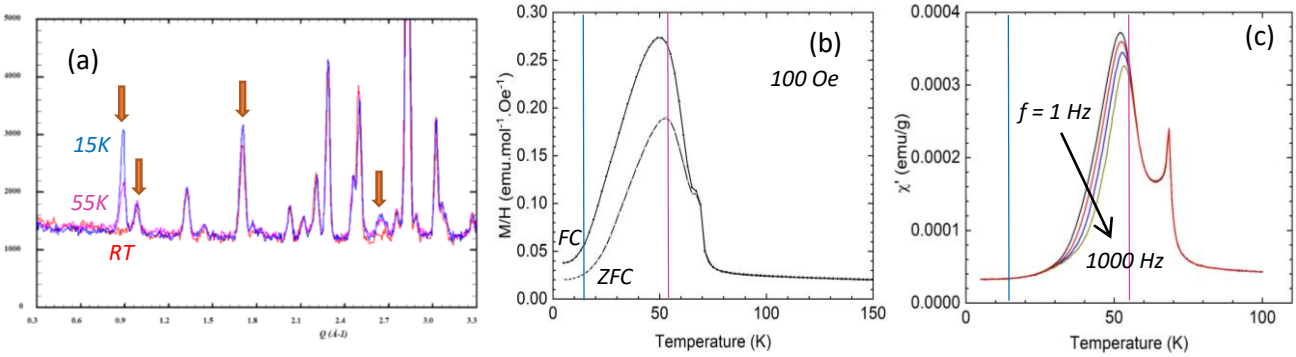

Figure 2: (a) NPD patterns of $Ni_4Nb_{1.8}Ti_{0.1}W_{0.1}O_9$ recorded at RT (red), 55 K (pink) and 15 K (blue); temperature dependence of the magnetic susceptibility: dc, zero field cooling and field cooling modes (b) and ac using 4 frequencies (c).

The analysis of these data is clearly in its early stages. Nevertheless, the preliminary tests using the *Fd'd'2* and *Fd'd2'* magnetic space groups, and same magnetic and crystallographic cells, are promising.

Since the x = 0.05 compound corresponds to a mixture of two close phases, i.e. the large *Fdd2* one and the parent small *Pbcn* one, these data will be used to understand the moving from one structure to the other one and to identify the origin of the super structure.

Quantitative in-situ analysis of nano-scale precipitates during ageing heat treatment of additively

Neutron Physics Laboratory - Neutron diffraction

Ahmad Kermanpur

Proposal ID

506

Quantitative in-situ analysis of nano-scale precipitates during ageing heat treatment of additively manufactured IN718 Ni-based superalloy

Ahmad Kermanpur and Peter Hedström, KTH Royal Institute of Technology, Sweden
Vasyl Ryukhtin, Nuclear Physics Institute, Řež, Czech Republic

Temporal evolution of the nano-scale strengthening precipitates during double-stage ageing heat treatment of the laser powder-bed fusion (LPBF) additively manufactured IN718 Ni-based superalloy is studied by small-angle neutron scattering (SANS) experiments. The rectangular specimens ($10\times10\times2$ mm^3) were investigated both *ex-situ* at room temperature and *in-situ* using a vacuum furnace following the ageing treatment. The thermal cycle consisted of a solution treatment at 1060 °C for 1 h followed by a double-stage ageing at 760 °C for 10 h, furnace-cooling, and 650 °C for 8 h, followed by air-cooling. The desired instrumental resolution spanned a scattering vector (Q) range of $0.02<Q<0.2$ nm^{-1} at a constant incident neutron wavelength of 0.209 nm, corresponding to scattering features with sizes from about 30 nm up to 300 nm in real space. The *ex-situ* measurements of the wrought and LPBF IN718 superalloy samples were first carried out with full statistics for 3.5 h. The *in-situ* SANS were conducted during ageing treatment of solution treated samples with a 20 min acquisition repetition at low instrumental resolution. The raw data were treated by standard procedure using "empty furnace" and "cadmium" scattering corrections. A simple spherical model with log-normal size distribution was used for fitting of precipitates. The fitting was done using SASProFit software.

The *ex-situ* SANS data of the LPBF and wrought samples are shown in Fig. 1. The observed increase of the SANS intensity in the aged samples compared to the solution treated ones, is caused by nucleation and growth of the nano-scale γ′′ (Ni_3Nb) and γ′ (Ni_3Al) precipitates. Neutron scattering length densities (SLD) of the γ′ and γ′′ phases as empirically calculated using compositions of TC-PRISMA simulations are very close (*i.e.* $SLD^{\gamma'}= 7.5177\times10^{10}$ Å^{-2}, $SLD^{\gamma''}= 7.5388\times10^{10}$ Å^{-2}). Therefore, these precipitates are practically indistinguishable by SANS. The differences in SANS scattering of the aged and solution treated samples in the high Q region were supposed to be caused by γ′′ and γ′ precipitates and therefore used for fitting using spherical models with log-normal size distribution. The fitted volume fraction of γ′′ and γ′ particles is higher for wrought (26.6 ± 0.19 %) than for LPBF (10 ± 3.5 %) alloy. However, these results are distorted by the instrumental limitation of the highest measured angle $Q_{max} \approx 0.2$ nm^{-1} which corresponds in real space to a minimum size which is possible to detect of $R_{min} \approx 15$ nm. Nevertheless, in the given windows, the wrought material after heat treatment contains more than twice higher particle volume fraction than the aged LPBF alloy. In fact, growth rate of the γ′′ precipitates is faster in the wrought material than in the LPBF one. The SANS data from the solution treated LPBF is higher than for the corresponding wrought one, obviously due to higher population of scattering particles like MC carbides and Laves phases.

Total counts of *in-situ* SANS raw data in dependence on ageing time are shown in Fig. 2. Monotonic increasing of scattering at 760 °C is caused by nucleation and growth of the precipitates and corresponds to increasing of their volume fraction in the covered size range. Interestingly, SANS total counts within statistical error remain constant during the second stage of ageing (at 650 °C during 10-18 h) due to stable volume fraction.

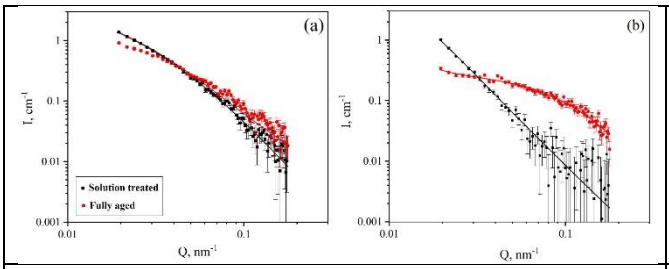

Fig. 1. *Ex-situ* SANS data for the (a) LPBF and (b) wrought samples in both solution treated and aged conditions.

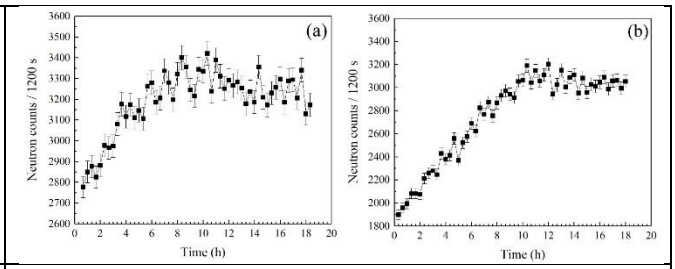

Fig. 2. *In-situ* SANS raw data during ageing treatment of the (a) LPBF and (b) wrought samples.

The *ex-situ* SANS data showed that the growth rate of the nano-scale precipitates is faster in the wrought material than in the LPBF one. The *in-situ* SANS data showed that the volume fraction of the nano-scale precipitates monotonically increases during the first stage of ageing and stagnates during the second stage. This information, which has not been reported before, suggests that a shorter ageing treatment compared to the standard cycle presented for the conventional alloy might be applicable for ageing the LPBF IN718 superalloy.

Interface characterization of Li metal / Lipon batteries

Neutron Physics Laboratory - Nuclear analytical methods with neutrons

Ralph Gilles

Proposal ID

573

Report regarding proposal ID 573: “Interface characterization of Li metal / Lipon batteries”

Ralph Gilles, Technical University of Munich (TUM), Germany
Andrew Westover, Katie Browning, Oak Ridge National Lab, USA
Antonino Cannavo, Jiri Vacik, G. Ceccio, Nuclear Physics Institute in Rez, Czech Republic

The experiments were carried out with the NDP spectrometer at the Nuclear Physics Institute (NPI) in Rez, Czech Republic, which is a part of the Center of Accelerators and Nuclear Analytical Methods (CANAM). The performed experiment deals with the study of interface between Li metal and Lipon layer to understand better the interface between the solid electrolyte Lipon and Li metal. Previous experiments show the problem of oxidation if Li metal layer was on top of the Lipon layer. Two strategies were followed to overcome this problem. First, the stacking sequence was changed that Lipon was on top and Li metal below as Lipon is less reactive with air than Li metal. To understand better the interface of Li metal and Lipon, an artificial layer was implemented between the two layers to split better the single signals from Li metal and Lipon. The idea was to use single layer information to understand better the interface region of Li metal and Lipon. In addition, AFM measurements were carried out to observe if surface oxidation occurs (due to oxidation, there is a significant increase in surface roughness, from which the degree of surface oxidation can be inferred).

The focus was on two kind of sample sets. First stack consists of i. Li~400 nm ii. Ni–50 nm, iii. Lipon-100 nm and the substrate sapphire -1 mm. The second stack is layered with i. Li~400 nm, Ni-50 nm and iii. Lipon-500 nm and sapphire -1mm.

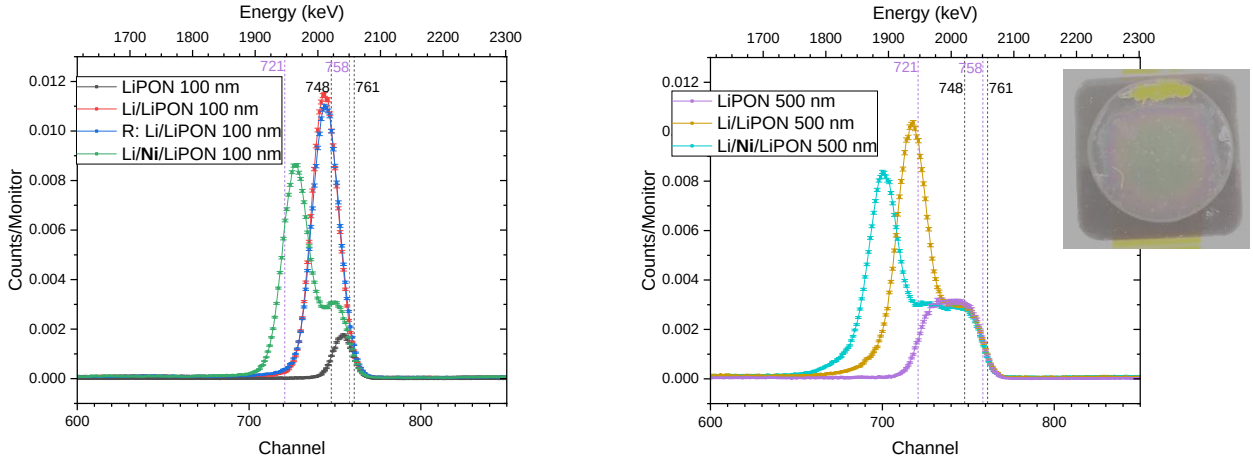

Fig. 1 The layer stacks with different Lipon thickness of 100 nm and 500 nm are compared with NDP measurements showing the influence of Ni interlayer and Lipon on Li metal layer. AFM image proofs no oxidation on the surface.

First results confirm the expected Lipon thickness of 448 nm (500 nm) and 95 nm (100 nm) assuming an atomic density of 7.81 x 10^{22} [at./cm^3] for Lipon. The Lipon layer on the top and Li below avoid the oxidation on the surface proofed with AFM technique. A mixed layer for the Li metal / Lipon stack was detected but a first fitting model for the Li metal / Ni / Lipon stack failed as Li diffusion takes place in the Ni layer. An exchange of the Ni layer with another metal with higher stability against Li diffusion could help to distinguish better the influence of single layer Li metal and Lipon using NDP in comparison to the bilayer Li metal / Lipon.

Using neutron diffraction to characterize bulk texture in additively manufactured magnesium alloy

Neutron Physics Laboratory - Neutron diffraction

Lisa Larsson

Proposal ID

574

Report regarding proposal "Using neutron diffraction to characterize bulk texture in additively manufactured magnesium alloy"

Additive manufacturing by powder bed fusion laser beam (PBF-LB) has opened up new possibilities in the manufacturing of biodegradable magnesium (Mg) alloys. Due to the unique thermal history of the process, the resulting part typically present anisotropic properties and texture. In terms of mechanical properties, the build direction does have a large impact on the final WE43 alloy specimens (Fig. 1). The laser scan strategy slightly alters alloy microstructure, but only has a minor effect on the mechanical response of the Mg-parts, which is in contrast to other metals manufactured by PBF-LB (e.g. [3]). We hypothesized this to be due to changes resulting grain orientations and texture in the direction of loading when it comes to the effect of build direction, and limited grain growth between layers minimizing the effect of scan strategy on resulting properties.

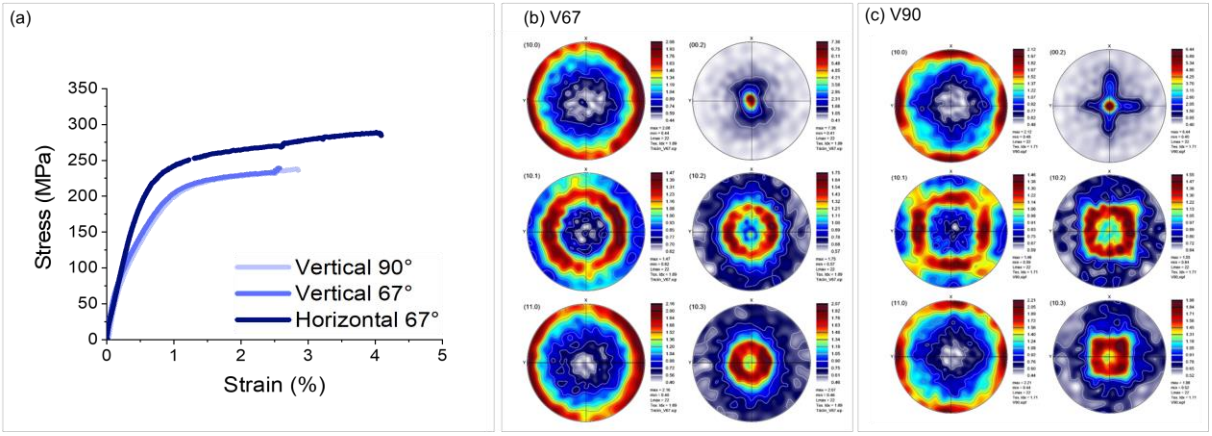

Figure 1. (a) Stress-strain curve for horizontally built samples and vertically built samples, and two different scan strategies. (b) Calculated neutron pole figures showing preferential crystallographic grain orientations, for the vertically printed samples when the scanning vectors are rotated 67°, and (c) 90° degrees between each scanned layer.

To determine the bulk texture of the as-printed components (Figure 1a), neutron diffraction was used to measure a large sample volume of 10 mm diameter cylinders. This ensures that observations are representative of the whole sample. Samples were fixed on the Euler goniometer and rotated along φ (0–360°) and χ (0–90°) angles with a step of 5°. Variation of neutron diffracted intensities for 6 individual reflections [(100), (002), (101), (102), (110) and (103)] were collected for each orientation on the MEREDIT instrument, using a neutron wavelength of 1.46 Å. The data was analysed using ATEX software. The orientation distribution function (ODF) was calculated for each sample, and pole figures for predefined reflections were calculated for easy comparison of all samples.

Some of the pole figures calculated from the neutron diffraction measurements are presented in Figure 1b and 1c. The sample printed with a 67°-rotation scan rotation shows higher intensity with more pronounced basal texture (i.e. a fiber texture with strong "out of plane" texture along the c-axis but no "in-plane" texture). For the sample printed with 90° rotation between layers it is observed that it is affecting also the "in-plane" texture. A cross-like pattern is observed for the (002)-pole and a square-like pattern for the (101)-pole, which relates to the 90° pattern that the laser shifts between layers. The degree of texture is, however, much smaller in-plane than out of plane. These results show the possibility of tuning both in-plane and out of plane texture by controlling sample orientation and scan strategy for LPBF of Mg alloy WE43. A more detailed analysis of how solidification and grain growth is influenced by the laser scanning pattern is currently being performed and a possible future experimental proposal.

References

[1] Jithin James Marattukalam et al., 2022. Materials Design. The effect of laser scanning strategies on texture, mechanical properties, and site-specific grain orientation in selective laser melted 316L SS

Two-dimensional waveguides in glass created by multi-energetic ion implantation via photoresist mask

Laboratory of Tandetron

Romana Mikšová

Proposal ID

575

Report regarding proposal "Two-dimensional waveguides in glass created by multi-energetic ion implantation via photoresist mask"

Romana Mikšová [1]*, Pavla Nekvindová[2], Petr Aubrecht[3], Anna Macková[1,4]

[1]*Nuclear Physics Institute CAS, Hlavní 130, 250 68 Rez, Czech Republic*
[2]*Department of Inorganic Chemistry, University of Chemistry and Technology in Prague, 166 28 Prague, Czech Republic*
[3]*Centre for Nanomaterials and Biotechnology, Faculty of Science, Jan Evangelista Purkyně University in Ústí nad Labem, 400 96 Ústí nad Labem, Czech Republic*
[4]*Department of Physics, Faculty of Science, University of J. E. Purkyně, Pasterouva 3544/1, 400 96 Ústí nad Labem, Czech Republic*

In the presented study the fabrication of optical waveguides in various silicate glasses (S-1, Gil11, BK7) using the single and multi-energy implantation of C^+ ions via photoresist mask (Fig. (a) and (b)). The elemental composition of pristine glasses and photoresist mask was determined using RBS method with 2 MeV He ion before implantation (Fig. (c)). These parameters were used for precise simulation of projected range in glasses.

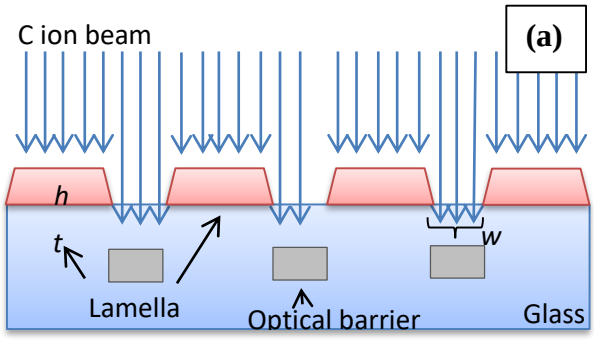

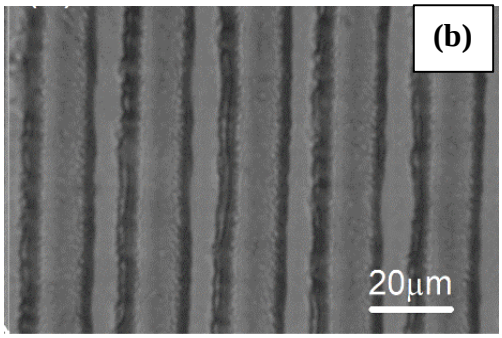

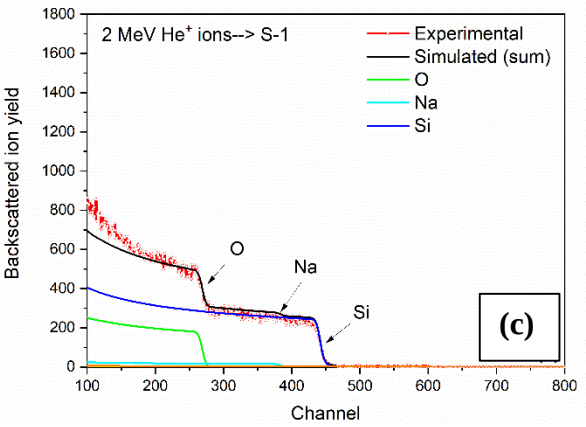

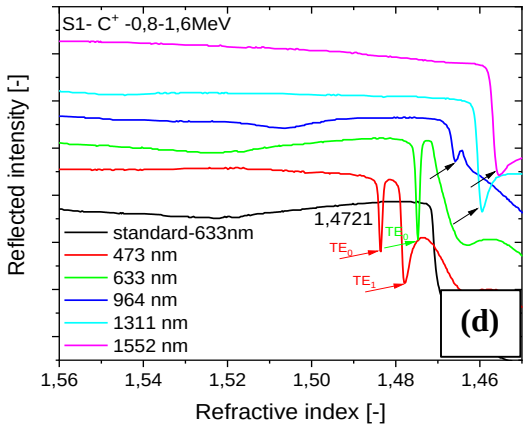

The optical modes are significant in S-1 glass where the range of the carbon ions is expected to be the deepest and hence the layer is the widest. Also obvious is the difference between multi and single-energy implantation, where at 473 nm only one mode of light propagates for single C ions implantation and two modes for sequential implantation (Fig. (d)). In the other two types of glass (GIL11 and BK7) either less or no number of modes is seen even at low wavelengths. This trend corresponds very well with the predicted depth of carbon projected range and takes with the indicated difference between multi and single-energy implantation. The properties of the glass substrate were in line with our assumptions. The glass S-1 with the highest content of silicate network showed the lowest density, and the glass BK7 containing Ba^{2+} ions as a modifier showed the highest density.

The results will be presented at European conference on applications of surface and interface analysis 2024 and published in Surface and Interface Analysis proceedings in the July of 2024.

Preparation of the Ni binary layers suitable for the formation of graphene

Laboratory of Tandetron

Romana Mikšová

Proposal ID

519

Report regarding proposal "Preparation of the Ni binary layers suitable for the formation of graphene"

Romana Mikšová [a], Adéla Jagerová[a,b], David Poustka[c], Anna Macková[a,b]*

[a]Nuclear Physics Institute CAS, 250 68 Rez, Czech Republic; [b]Department of Physics, Faculty of Science, University of J. E. Purkyně, Pasterouva 3544/1, 400 96 Ústí nad Labem, Czech Republic; [c]Centre for Nanomaterials and Biotechnology, Faculty of Science, J. E. Purkyně University in Ústí nad Labem, Pasteurova 3544/1, 400 96 Ústí nad Labem, Czech Republic

Thin bimetallic Ni-Au layers (~100 nm) with three different Au content were prepared by direct current magnetron sputtering onto sapphire substrates. The elemental composition and the layer thickness of bimetallic layers were controlled during the sputtering process. The prepared Ni-Au layers were annealed at temperatures of 400°C and 900°C in the air to determine the behaviour of Au and Ni in the layers after heating. The elemental composition and depth profiling was provided by Rutherford backscattering spectrometry (RBS) (Figure a). The surface morphology was examined via Scanning electron microscopy (SEM).

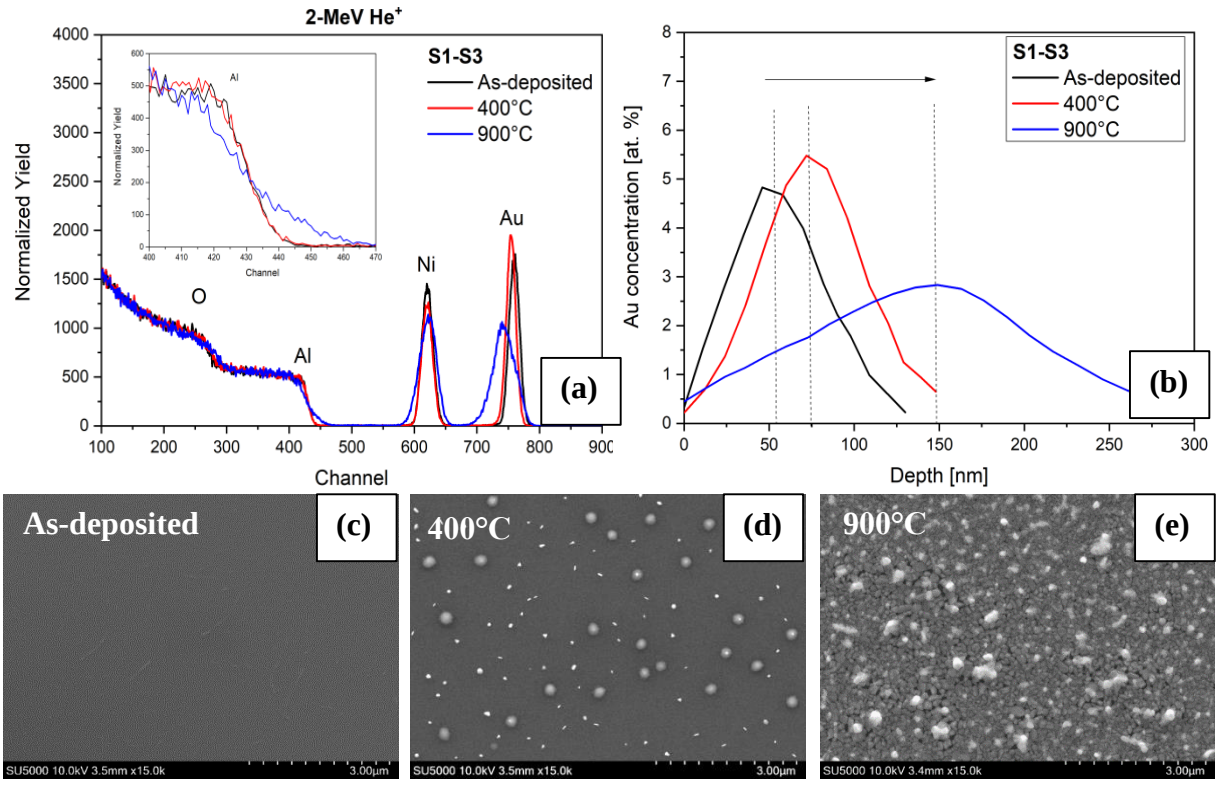

RBS measurements show Au and Al_2O_3 inter-diffusion, especially after annealing at 900°C (Figure b – blue line). Blister formation is shown in sputtered Ni-Au thin layer after annealing (Figures d and e) which is connected to the out-diffusion of the trapped sputtering gas after thermal annealing. It is shown that blister size is reduced by increasing the sputtering pressure. Changes in the surface morphology are connected to the formation of grain and voids, where increasing the Au content in the layers results in larger grain on the sample surface.

The part of the results was published published in Radiation Effects and Defects in Solids. The next manuscript will be published in Vacuum at the beginning of 2023.

Ex-situ & in-situ neutron diffraction study of deformation mechanism in Ti modfiied with trace B

Neutron Physics Laboratory - Neutron diffraction

Gergely Németh

Proposal ID

455

Report regarding proposal “Ex-situ & in-situ neutron diffraction study of deformation mechanism in Ti modfiied with trace B”

Gergely Németh, Faculty of Mathematics and Physics, Charles University

Ex-situ and in-situ neutron diffraction experiments were performed on 6x, 8x and 12x hot rolled commercially pure titanium grade 2 specimens modified by 0.1, 0.2 and 0.5 wt. % boron. The additional boron forms TiB monocrystal whiskers in pure Ti and the prepared material can be considered as discontinuously-reinforced metal matrix composite (DRMMC) which can have a relatively large to a moderate effect on mechanical properties depending on the elastic properties, shape, spatial arrangement and volume fraction of the reinforcement phase.

During the ex-situ measurement, neutron diffraction line scanning technique was used to study the residual stress (RS) distribution across the thickness of the rolled samples. First, the residual strain distribution was studied in three mutually perpendicular directions, denoted as LD (Longitudinal or rolling direction), TD (Transversal dir.) and ND (Normal dir.), corresponding to the main directions of the rolled plates. To increase the resolution (modification of the original proposal) and to have almost the same step-density, the step sizes were 0.5 mm, 0.45 mm and 0.3 mm for 6x, 8x and 12x rolled samples, respectively. Exposure times to collect the neutron diffraction signals from 0.1% B - 0.2% B and 0.5%B were 75 minutes and 100 minutes, respectively. Pseudo strains near the edge of the samples were treated according to [1].

The effect of the increased boron content on the RS distribution is most obvious after 12x rolling, as can be seen from Fig. 1. 0.1% B shows almost typical RS distribution for rolled monolithic material with local minimum in the center while in the case of 0.5% B, RS has local maximum in the same position.

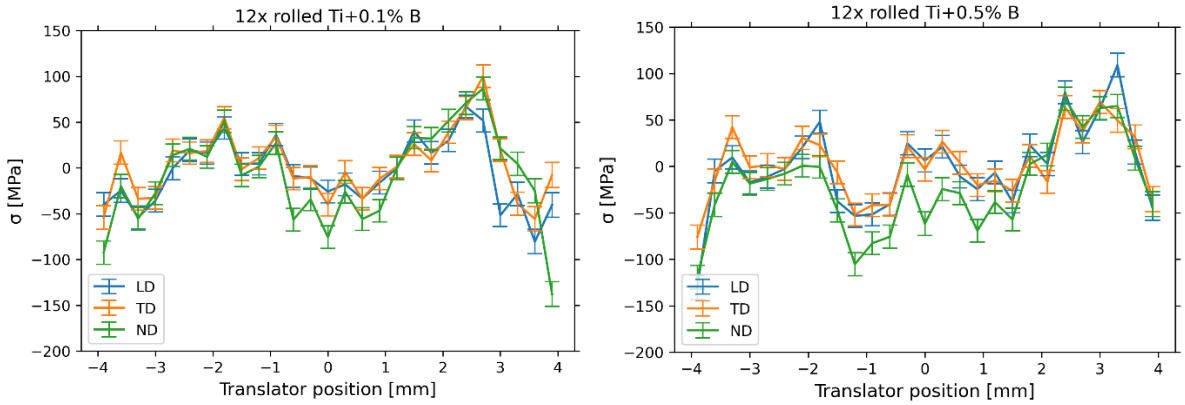

Fig. 1. Residual stress distribution in samples 12x hot rolled with B contents 0.1 wt. % and 0.5 wt. %

In-situ measurements were carried out only on 5 samples, since the deformation rig and the whole system had shown instability and many experiments had to be repeated several times without any reasonable outcome.

On the other hand, ex-situ measurements show valuable results and their publication is expected within a few months.

References:

[1] J. Šaroun, J. Rebelo-Kornmeier, J. Gibmeier, M. Hofmann, Treatment of spatial resolution effects in neutron residual strain scanning, Phys./B. 551 (2018) 468–471, https://doi.org/10.1016/J.PHYSB.2018.01.013.